Article

Stepwise activation of a metabotropic glutamate receptor

https://doi.org/10.1038/s41586-024-07327-x

Received: 28 August 2023

Accepted: 15 March 2024

Published online: 17 April 2024

Check for updates

Kaavya Krishna Kumar[1,9]✉, Haoqing Wang[1,2,9], Chris Habrian[1], Naomi R. Latorraca[3], Jun Xu[1], Evan S. O'Brien[1], Chensong Zhang[4], Elizabeth Montabana[1], Antoine Koehl[1,5], Susan Marqusee[3,6,7], Ehud Y. Isacoff[3,8] & Brian K. Kobilka[1]✉

Metabotropic glutamate receptors belong to a family of G protein-coupled receptors that are obligate dimers and possess a large extracellular ligand-binding domain that is linked via a cysteine-rich domain to their 7-transmembrane domain[1]. Upon activation, these receptors undergo a large conformational change to transmit the ligand binding signal from the extracellular ligand-binding domain to the G protein-coupling 7-transmembrane domain[2]. In this manuscript, we propose a model for a sequential, multistep activation mechanism of metabotropic glutamate receptor subtype 5. We present a series of structures in lipid nanodiscs, from inactive to fully active, including agonist-bound intermediate states. Further, using bulk and single-molecule fluorescence imaging, we reveal distinct receptor conformations upon allosteric modulator and G protein binding.

Metabotropic glutamate receptors (mGlus) belong to a family of obligate dimeric G protein-coupled receptors (GPCRs), which are activated by the excitatory neurotransmitter L-glutamate[1]. Each protomer contains a large extracellular ligand-binding domain that is made up of a Venus fly trap (VFT) domain, which contains the orthosteric ligand binding site, and a cysteine-rich domain (CRD). The CRD connects the VFT to the family-defining 7-transmembrane domain (TMD)[1] (Extended Data Fig. 1a). The binding of glutamate causes the closure of the VFTs and a protomer rearrangement that brings the CRDs and TMDs into proximity[2]. Dimerization of the mGlus is mandatory for their function, and the rearrangement upon activation of the receptors is a complex allosteric process with the two protomers influencing each other[3]. Allosteric modulators of mGlus bind the TMD[4] to regulate signalling by themselves or in conjunction with orthosteric ligands. Ultimately, agonists and positive allosteric modulators (PAMs) activate mGlus by stabilizing intermolecular interactions between the protomers which enable G protein coupling to the TMD.

To better understand the activation mechanism of mGlus, and to delineate the allosteric link between ligands and G proteins, we took mGlu5 as a representative of the mGlu family and employed a combination of structural and biophysical techniques to characterize the conformational landscape of receptor activation. We first show the importance of a lipid bilayer for mGlu5 activation. To comprehensively understand the receptor activation pathway, we determine structures of mGlu5 in the presence of a small molecule orthosteric agonist and an allosteric modulator, as well as the allosteric nanobody, Nb43 (ref. 2). As a pure PAM, Nb43 potentiates the activity of orthosteric agonists but lacks intrinsic activity of its own. In the presence of the orthosteric agonist L-quisqualic acid (Quis) and Nb43, we resolved two receptor conformations: (1) an intermediate (intermediate 1a, Fig. 1a) with the VFT upper lobes closed but a large interprotomer distance, reflecting an inactive conformation; and (2) an 'active-like' structure (intermediate 2a, Fig. 1a) in which the VFT lower lobes, CRDs and the TMDs are in close proximity. It should be noted that for the purpose of discussion, all conformations between Apo and G protein-bound 'fully active' are named 'intermediates'. Addition of agonist-PAM 3-cyano-*N*-(1,3-diphenyl-1*H*-pyrazol-5-yl)benzamide (CDPPB) to the Quis- and Nb43-bound mGlu5 fully stabilized a single active conformation (intermediate 3a, Fig. 1a) that resembles the Quis- and Nb43-bound intermediate 2a structure. Interestingly, in this complex we observe an asymmetric action of CDPPB, with density supporting its binding to only one of the two TMDs, as opposed to a structure of mGlu5 with CDPPB alone, but without Quis or Nb43, for which we observe CDPPB in both TMDs (intermediate 1b, Fig. 1a). We further investigate the intersubunit conformational changes upon ligand and G protein binding using bulk fluorescence spectroscopy and single-molecule Förster resonance energy transfer (smFRET). We observe receptor conformations that correlate well with the determined structures as well as several receptor conformations that are uniquely observed in biophysical studies, including states stabilized by CDPPB (intermediates 2b and 3b, Fig. 1a) and one stabilized by G protein (fully active). Finally, combining all the data, we propose a model for the stepwise activation of mGlu5. Figure 1a gives an overview of the model developed from the results presented in this manuscript.

Lipids critical for mGlu5 activation

To identify the best conditions for studying mGlu5 activation, we monitored the ability of mGlu5 to drive guanosine-5′-triphosphate (GTP) turnover via the heterotrimeric G protein, G_q, in detergent micelles and

[1]Department of Molecular and Cellular Physiology, Stanford University School of Medicine, Stanford, CA, USA. [2]Sarafan ChEM-H, Stanford University, Stanford, CA, USA. [3]Department of Molecular and Cell Biology, University of California, Berkeley, Berkeley, CA, USA. [4]Division of CryoEM and Bioimaging, Stanford Synchrotron Radiation Lightsource, SLAC National Accelerator Laboratory, Menlo Park, CA, USA. [5]Electrical Engineering and Computer Sciences, University of California, Berkeley, Berkeley, CA, USA. [6]QB3 Institute for Quantitative Biosciences, University of California, Berkeley, Berkeley, CA, USA. [7]Department of Chemistry, University of California, Berkeley, Berkeley, CA, USA. [8]Helen Wills Neuroscience Institute, University of California, Berkeley, Berkeley, CA, USA. [9]These authors contributed equally: Kaavya Krishna Kumar, Haoqing Wang. ✉e-mail: kaavyak@stanford.edu; kobilka@stanford.edu

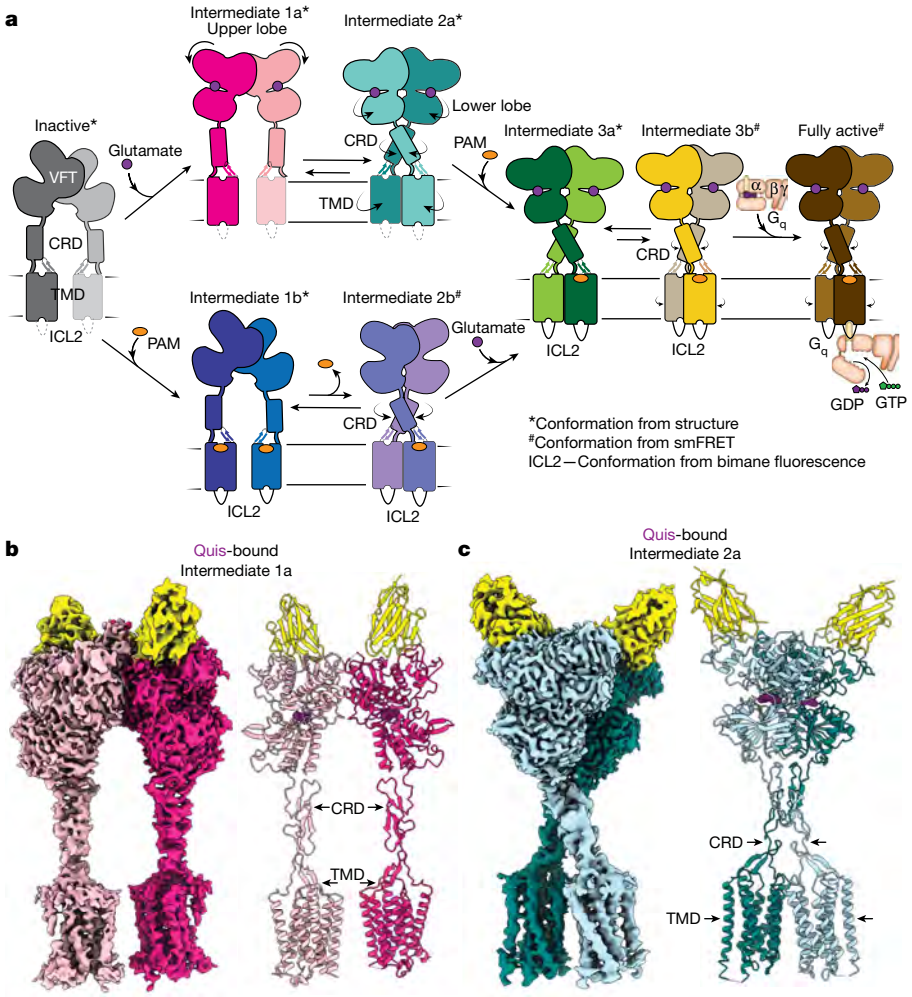

Fig. 1 | Sequential activation of mGlu5 in lipid environment. a, Using the data from this study we propose a model for mGlu5 activation. The addition of an orthosteric agonist (for example, glutamate) results in the closing of the upper lobe (intermediate 1a). This conformation is in equilibrium with a conformation in which the twisting of the lower lobe brings the CRDs and TMDs into proximity (intermediate 2a). The addition of a PAM stabilizes the CRDs and TMDs, including intracellular loop 2 (ICL2), in an active conformation (intermediate 3a). Intermediate 3a is in equilibrium with intermediate 3b, which is characterized by a smaller intersubunit distance. In the presence of an orthosteric agonist, the PAM binds to one protomer (intermediates 3a and 3b), whereas in its absence the PAM binds to both the protomers symmetrically (intermediate 1b). Further addition of G protein to the agonist and PAM-bound mGlu5 results in the stabilization of a unique fully active conformation of the receptor (fully active). **b**, Cryo-EM density and model of Quis-bound mGlu5 in nanodisc, representing an intermediate 1a state, in which Quis is bound to the VFTs; however, the CRDs and TMDs are far apart, mimicking the inactive state. VFT binding Nb43 is shown in yellow. **c**, Cryo-EM density and model of nanodisc-incorporated Quis-bound mGlu5, intermediate 2a state. The CRDs and TMDs are in an active conformation (close together).

reconstituted in lipid nanodiscs using the belt protein MSP2N2 (about 16 nm diameter)[5] and a 1-palmitoyl-2-oleoyl-glycero-3-phosphocholine (POPC)/1-palmitoyl-2-oleoyl-sn-glycero-3-(phospho-rac-(1-glycerol)) (POPG) lipid mixture (Extended Data Fig. 1b). In detergent micelles, we observed no activation of G_q by mGlu5 bound to Quis, and only minimal activation (about 20% above G_q alone) by mGlu5 bound to both Quis and CDPPB (Extended Data Fig. 1c), whereas the M1 muscarinic receptor in detergent micelles was able to efficiently activate G_q (Extended Data Fig. 1d). By contrast, mGlu5 in lipid nanodiscs was able to robustly activate G_q by Quis alone or Quis and CDPPB[6] (Extended Data Fig. 1c). To assess whether this dependence on lipid environment for mGlu5 activation is a consequence of alteration in receptor conformation, rather than a direct effect of lipid on either G_q activation or mGlu5 affinity for ligand, we performed hydrogen–deuterium exchange monitored by mass spectrometry (HDX-MS). Upon agonist binding to mGlu5 in detergent, we observe differences in the deuterium uptake in the VFT consistent with ligand binding[2] (Extended Data Fig. 2a,b). Peptides in the VFT of agonist-bound mGlu5 exhibit nearly identical behaviour in detergent and in nanodiscs (Extended Data Fig. 2a,b). Thus, the effects of agonist binding on the VFT do not seem to depend on the receptor TMD environment. However, there are notable differences in the TMD of agonist-bound mGlu5 between detergent and nanodiscs: specifically, peptides in the intracellular region of transmembrane (TM) 3 exhibit reduced deuterium uptake in nanodiscs compared with in detergents (Extended Data Fig. 2c). In other mGlus, for example, in mGlu2, on the basis of cryogenic electron microscopy (cryo-EM) structures this region of TM3 undergoes conformational changes upon interacting with G protein[7] (Extended Data Fig. 2d). Taken together, these data are consistent with a model in which lipids modulate the ability of mGlu5 to adopt an active state capable of GTP turnover.

Quis-bound mGlu5 adopts two conformations

To better understand the activation mechanism of mGlu5, we determined the structure of Quis- and Nb43-bound mGlu5 reconstituted into lipid nanodiscs using single-particle cryo-EM. Data processing

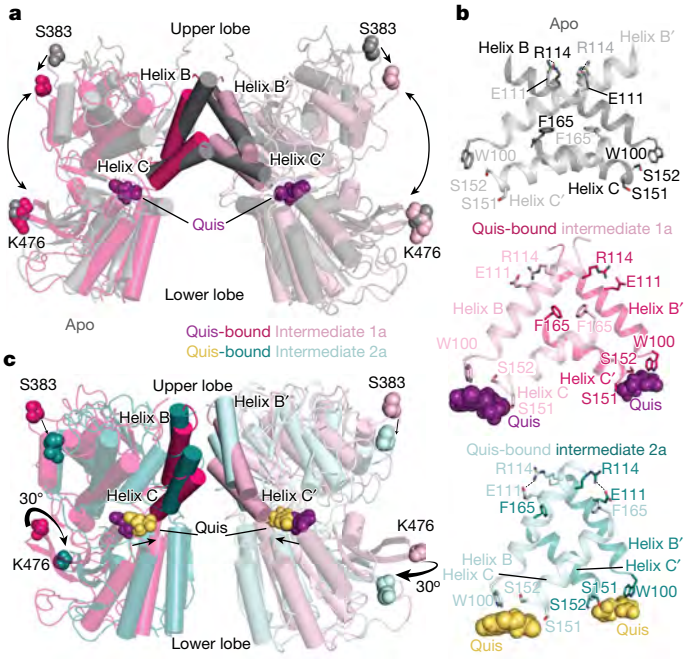

Fig. 2 | Structures of Quis-bound conformations of mGlu5 in nanodisc. **a**, VFTs of Apo (grey, PDB 6N52) and Quis-bound intermediate 1a are overlayed. Upon Quis binding the upper lobe closes, as seen by the movement of S383, whereas not much change is seen in the lower lobe (comparing K476 between the structures). Also shown is the comparison of the B and C helices at the intersubunit interface in the Apo and Quis-bound intermediate 1a state. **b**, The intersubunit rearrangement upon Quis binding reorients the B and C helices leading to a reduction in the helix angle. Top, Apo; middle, Quis-bound intermediate 1a; bottom, Quis-bound intermediate 2a. Residue R114 interacts with E111 from the adjacent protomer in the Apo state and within the same protomer in the Quis-bound intermediate 2a. The residue F165 is shown to illustrate the change in the position of the C helix. There is a downward movement of W100 towards Quis in intermediates 1a and 2a. Owing to the lower lobe rotation in intermediate 2a, a further inward movement of Quis is seen. **c**, Overlay of VFTs of Quis-bound intermediate 1a and Quis-bound intermediate 2a, showing a small change in the upper lobe (movement of S383). The lower lobes twist 30° and move closer together as seen by comparing K476 between the structures. The B and C helices at the protomer–protomer interface in the Quis-bound intermediate 2a state show an upward shift compared with the Quis-bound intermediate 1a. This is probably the result of the inward movement of Quis (from purple to yellow) and the rearrangement of the lower lobe.

revealed two distinct conformations of the receptor (Extended Data Fig. 3). Although both structures have Quis bound (to both protomers), one shows an 'intermediate' conformation (intermediate 1a, Fig. 1a), wherein the VFTs are closed, but CRDs and TMDs are far apart as in the inactive mGlu5 structure (Fig. 1b and Extended Data Fig. 4a), whereas the other conformation is 'active-like' (intermediate 2a, Fig. 1a), such that the CRDs and TMDs are close together, forming the TM6–TM6 interface, the hallmark of Family C activation[2] (Fig. 1c).

To investigate changes accompanying Quis binding, we compared the previously determined Apo (Protein Data Bank (PDB) code 6N52 (ref. 2)) structure with the current Quis-bound, intermediate 1a structure (Extended Data Fig. 4a). Upon Quis binding, there is a decrease in distance between the upper and lower lobes of the VFT (Fig. 2a). This decrease is mostly due to the closure of the upper lobe (Fig. 2a and Extended Data Fig. 4b). The upper lobe closure is accompanied by some rearrangements in the lower lobe and the 'hinge region' (the region between the lobes in the dimer interface) (Extended Data Figs. 1a and 4b). For example, changes to Quis-interacting residues such as W100 and E279 (Fig. 2b and Extended Data Fig. 4a) result in conformational changes in the B and C helices at the intersubunit interface (Fig. 2a,b). Hindrance to the movement of these residues appears to stabilize the receptor in an inactive conformation, as seen in the antagonist-bound structure (PDB code 7FD9 (ref. 8)) (Extended Data Fig. 4c). Hence, changes in the lower lobe residues (for example, E279) and the hinge region trigger rearrangement of the upper lobe (that is, closing) upon Quis binding (Fig. 2a and Extended Data Fig. 4b).

To study the structural changes that occur subsequent to Quis binding to form the active state of the receptor, we compared the Quis-bound intermediate 1a (Fig. 1a) and the Quis-bound intermediate 2a (Fig. 1a) structures of mGlu5 (Fig. 1b,c). We observe a large 'twisting' of the VFT lower lobe in the intermediate 2a structure (Fig. 2c and Extended Data Fig. 4d). The lower lobe of the VFT moves as a rigid body and maintains the Quis binding pocket (root mean squared deviation (RMSD) approximately 0.5) (Extended Data Fig. 4e) and initiates the rearrangement of the B and C helices in the hinge region (Fig. 2b,c). These structural changes ultimately lead to the CRDs and TMDs (Extended Data Fig. 4f–i) moving close to each other (hallmark of Family C GPCR activation) to activate mGlu5.

Symmetric to asymmetric binding of mGlu5 PAM

Allosteric modulators of Family C GPCRs bind in the TM region and modulate orthosteric ligand binding and signalling. Crystal structures of single mGlu TMDs bound to negative allosteric modulators (NAMs) have been previously determined[9–12]. To gain structural insights into the activity of allosteric modulators in the context of the full-length receptor, we determined the structures of nanodisc-incorporated CDPPB-bound mGlu5 (and Nb43) in the absence and presence of Quis (Fig. 3a and Extended Data Figs. 5 and 6). In the absence of Quis, CDPPB-bound mGlu5 (intermediate 1b, Fig. 1a) adopts a conformation in which the protomers are separated, and we observe density for CDPPB in both TM protomers, indicating symmetric binding (similar to previously seen for mGlu bound to NAM[13,14]) (Extended Data Fig. 7). However, in the presence of Quis, CDPPB binds to the TMD of only one protomer[15] (that is, is bound asymmetrically) (Fig. 3a). Moreover, unlike Quis alone, with Quis and CDPPB we obtained only one conformation with the protomers close together (intermediate 3a, Fig. 1a and Extended Data Fig. 5), consistent with stabilization of the active conformation (Extended Data Fig. 8a,b).

Asymmetric allosteric modulator binding to only one protomer TMD is seen in other Family C GPCRs[7]. Molecular dynamics simulations were performed to validate CDPPB pose (Extended Data Fig. 9). CDPPB interacts similarly to the mGlu5 NAM MPEP (PDB code 6FFI (ref. 11)), with the exception of a large outward motion of W785$^{6.50}$ (Fig. 3b and Extended Data Fig. 8c) (superscript indicating GPCRDB canonical numbering scheme[16]). In the CDPPB-bound protomer, the entire TM6 is moved outward (C785$^{6.64}$ Cα–Cα approximately 3.5 Å), with Y779$^{6.44}$ pointing towards the protomer that does not contain CDBBP (Fig. 3c and Extended Data Fig. 8d,e). This appears to result in the inward movement of TM6 in the CDBBP-less protomer, with W785$^{6.50}$ occluding the PAM binding site (Extended Data Fig. 8f). This asymmetric PAM binding allows the protomer TMDs to form a tight interface. Other studies have also shown that the conformation of W785$^{6.50}$ is crucial for the stabilization of the active structure[8,17–20]. Mutation of W785$^{6.50}$ affects PAM affinity and cooperativity, with the W785$^{6.50}$A mutant increasing PAM (a CDPPB analogue was used in the study) cooperativity to glutamate for signalling[19,21]. Furthermore, mutations to CDPPB binding pocket residues, such as P654$^{3.40}$, Y659$^{3.44}$, T781$^{6.46}$, W785$^{6.50}$, F788$^{6.53}$, S809$^{7.39}$ and A810$^{7.40}$ (Extended Data Fig. 8f), have been shown to affect PAM affinity. Also, studies have shown that N747$^{5.47}$ is important for NAM binding and, perhaps, stabilizes the inactive state[18–20,22]. Compared with the inactive structure, in the CDPPB-bound structure, N747$^{5.47}$ moves away from CDPPB, possibly to stabilize an active structure (Extended Data Fig. 7b).

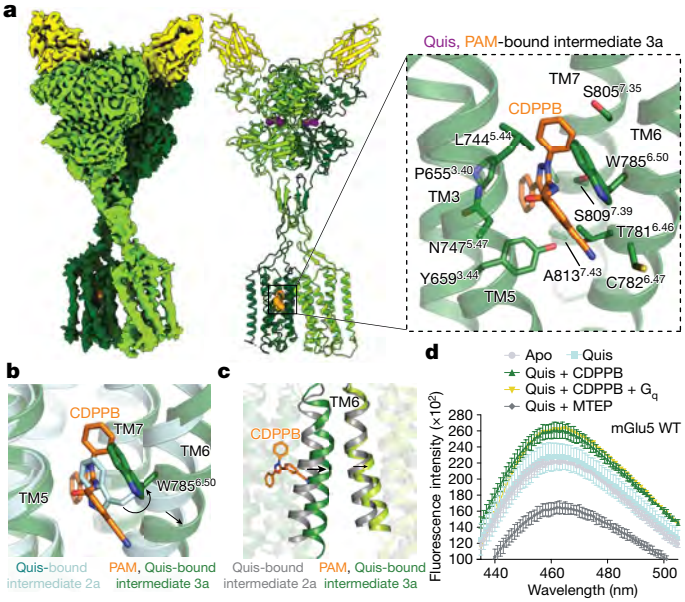

Fig. 3 | Structural changes upon PAM binding to mGlu5. a, Cryo-EM density and model of CDPPB (orange) and Quis-bound mGlu5 in a nanodisc. The structure represents the intermediate 3a state with the CRDs and TMDs in proximity. Nb43 is shown in yellow. Insert, binding pocket of CDPPB in the TM region showing residues within 4 Å as sticks. **b**, CDPPB binding to the TMD causes the rearrangement of W785$^{6.50}$ to accommodate the ligand. **c**, Comparing Quis-bound intermediate 2a and CDPPB, Quis-bound intermediate 3a structures show differences in the conformation of TM6 at the protomer interface. **d**, Bimane spectra of mGlu5 in nanodiscs labelled at positions C691$^{4.30}$ (end of TM4) and C681^{ICL2}. Adding Quis (cyan) results in no change in the spectra compared with Apo (grey). However, Quis and CDPPB increase the fluorescence (dark green), indicating a change in the ICL2 environment. Further addition of G_q does not result in a change in the bimane spectrum (yellow). The addition of Quis and MTEP causes a decrease in fluorescence. Data represented as mean ± s.d., $n = 3$ individuals. WT, wild type.

To tease out the differences between the Quis-bound intermediate 2a and CDPPB, Quis-bound intermediate 3a states, we carried out 3D Variability Analysis (3DVA)[23]. In both cases, we observed similar modes of variability (Supplementary Video 1), suggesting these are of biological relevance, rather than being artifacts resulting from overfitted noise in cryo-EM data. Notably, in the Quis-bound dataset, we detect a more pronounced 'stretch' motion between VFT and TMDs (Supplementary Video 1). Given that CDPPB binds the TMD, we hypothesize that CDPPB can 'lock' the TM–TM interface of mGlu5 homodimer in an active conformation, consistent with the role of CDPPB as a PAM. In addition, 3D Flexible Refinement (3DFlex)[24] revealed an asymmetric stretching pattern (Supplementary Video 2), wherein one protomer exhibited greater translational movement than the other. This indicates some asymmetry in the activation of the protomers in the presence of CDPPB, perhaps consistent with the observed asymmetric PAM binding (Fig. 3a).

Ligand alters ICL2 conformation

Previous structural studies of mGlu receptors have shown that ICL2 is stabilized in the presence of G protein[7,25]. To investigate conformational changes in ICL2 following ligand binding, we used the environmentally sensitive fluorophore monobromobimane (bimane) as a conformational reporter (Extended Data Fig. 10a–c). We performed bimane spectroscopy on two versions of nanodisc-incorporated mGlu5, the wild type, with two native cysteines, C681^{ICL2} and C691$^{4.30}$, labelled (Fig. 3d and Extended Data Fig. 10d), and mutant mGlu5, with only C681^{ICL2} labelled (Extended Data Fig. 10e,f). Notably, the two bimane-labelled constructs yielded similar results (Extended Data Fig. 10d,f). The addition of Quis alone did not produce a significant change (Fig. 3d and Extended Data Fig. 10d) in the bimane fluorescence spectrum, suggesting that an orthosteric agonist alone has a limited ability to stabilize an active conformation of TM intracellular loops. However, the addition of CDPPB to Apo- or Quis-bound mGlu5 increased fluorescence, indicating a change in the ICL2 environment (Fig. 3d and Extended Data Fig. 10d–f). Interestingly, compared with Quis alone, the structure of mGlu5 with Quis and CDPPB bound shows some changes in TM3 and TM4. These changes could be potentially contributing to changes in ICL2 (Extended Data Fig. 10g). No further change was observed with the addition of G_q (Fig. 3d). On the other hand, the mGlu5 NAM MTEP (with Quis or antagonist, LY341495) binding markedly decreased fluorescence intensity (Fig. 3d and Extended Data Fig. 10d–f). The decrease in fluorescence with the NAM could be due to bimane quenching by adjacent aromatic residues[26,27], such as, for example, when ICL2 residue Y757$^{5.57}$ approaches the TMD in the inactive conformation. This contrasts with the increase in fluorescence intensity in the presence of the PAM, CDPPB, when ICL2 may adopt an unquenched extended conformation (ICL2 in intermediates 1b, 2b, 3a and 3b in Fig. 1a). Hence, allosteric modulators seem to regulate ICL2 conformation.

Activation dynamics of mGlu5

Agonist binding to the VFT triggers TM rearrangements via the CRD. To investigate the mechanism of mGlu5 activation, we studied the conformational dynamics of the CRDs using smFRET[28,29]. smFRET has been used to study the VFT conformational changes upon glutamate binding[30]. We site-specifically labelled a single introduced Cys (in a minimal Cys background) (Extended Data Fig. 10a–c) in the CRD of each protomer at position 560, with cysteine-reactive versions of LD555 (donor) and LD655 (acceptor), to probe the distance between the CRDs as a measure of mGlu5 activation (Fig. 4a, Extended Data Figs. 11 and 12a and Supplementary Fig. 2).

In the Apo state, mGlu5 exhibits a dominant peak centred at a FRET efficiency of about 0.25 and includes a broad right skew to higher FRET values, around 0.4 and approximately 0.6 (Fig. 4b,d, grey). This low-FRET state at 0.25 is increased by the orthosteric antagonist LY341495 (Extended Data Fig. 12b). Further, with LY341495, a broad peak at 0.4 persists but the 0.6 peak disappears (Extended Data Fig. 12b). This indicates that the 0.25 and 0.4 FRET states correspond to inactive states of the receptor (Extended Data Fig. 12b and Supplementary Fig. 2). Upon Quis binding, there is a shift in the occupancy to a mid-FRET state, centred at 0.6 (Fig. 4b,d, cyan, and Extended Data Fig. 11). On the basis of the distance between residue 560 in each protomer in the different structures that we obtained, the low- and mid-FRET populations seem to correspond to the two distinct Quis-bound structures seen above (Fig. 1a): the intermediate 1a state (low-FRET) and the intermediate 2a state (mid-FRET) (Supplementary Fig. 2). mGlu5 incubated with CDPPB alone occupies a dominant peak at 0.25 (intermediate 1b, Fig. 1a) and a peak at 0.6 (intermediate 2b, Fig. 1a) (Extended Data Fig. 12c). Intermediate 2b was not detected by cryo-EM. In the presence of Quis and CDPPB, the 0.6 peak is dominant (intermediate 3a, Fig. 1a), with a decrease in the low-FRET state (Fig. 4b,d, dark green) and an emergence of a high-FRET peak at around 0.75 (Fig. 4b,d, dark green, and Extended Data Fig. 11). The centre of the low-FRET peak has shifted from 0.25 to 0.4 compared with Quis alone (Extended Data Fig. 11). This might imply that in the presence of Quis and CDPPB mGlu5 samples have higher FRET states, that is, active states, which could explain the single active structure with cryo-EM. Furthermore, the 0.75 peak corresponds to a distinct active-like state of the receptor (intermediate 3b, Fig. 1a) not seen in the cryo-EM structures. However, our 3DFlex analysis of the Quis and CDPPB cryo-EM dataset reveals conformations in which the CRDs of the homodimers are closer ('squeeze' motion) than that seen in the Quis structure (Supplementary Video 2), agreeing with

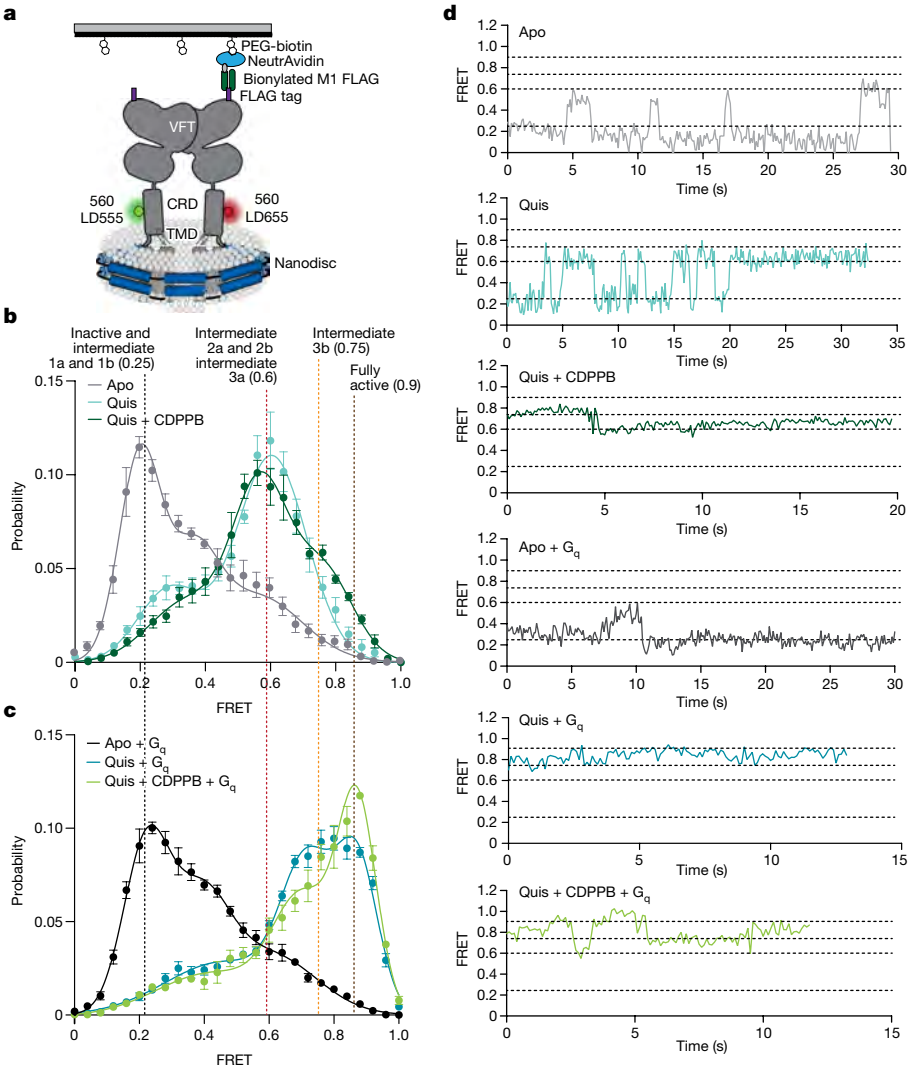

Fig. 4 | Ligand stabilized conformations of mGlu5 in nanodisc. a, A schematic representation of the smFRET experiment. **b**, In the Apo state (grey) a dominant inactive FRET peak at around 0.25 is observed ($n = 319$). The binding of the agonist, Quis, results in the appearance of an approximately 0.6 FRET state (intermediate 2a, cyan, $n = 392$) with a minor peak at 0.25 (intermediate 1a). The addition of CDPPB to Quis-bound mGlu5 stabilizes the 0.6 FRET state (intermediate 3a), decreases the occupancy of the 0.25 state and results in the appearance of a new FRET peak at around 0.75 (intermediate 3b, dark green, $n = 329$). High FRET peaks (the 0.6 and 0.75 peaks) represent the active state population of the receptor with the CRDs and TMDs in proximity. Histograms are shown with a three-Gaussian fit to the data, and represented as mean ± s.e.m. **c**, The coupling of G_q to Apo (dark grey, $n = 329$) remains largely unchanged compared with Apo alone (Fig. 4b), whereas the addition of G_q in the presence of Quis results in the near complete abrogation of the 0.6 FRET peak in favour of the 0.75 peak (intermediate 3b) and a new peak at around 0.9 (fully active) (teal, $n = 306$), which is further stabilized in the presence of CDPPB (light green, $n = 317$). Histograms are shown with a three-Gaussian fit to the data, and represented as mean ± s.e.m. **d**, Example FRET traces are shown for each ligand condition.

intermediate 3b. These observations indicate that the CRDs are dynamic, and that agonist and PAM binding progressively increases the occupancy of states in which the CRDs come into closer and closer contact, and suggest that our intermediate structures lie on this pathway. Moreover, the results show that PAMs actuate an allosteric back communication from the TMDs to the CRDs.

To study the effects of G protein on receptor conformational dynamics, we added G_q to Quis-bound mGlu5. The addition of G_q depletes the FRET peak at about 0.6 and shifts the receptor to inhabit the 0.75 FRET state observed in Quis and CDPPB, and a new FRET state at approximately 0.9 (Fig. 4c,d, teal). This higher FRET peak is also seen when G_q is added to CDPPB-bound mGlu5 (in the absence of Quis) (Extended Data Fig. 12c), agreeing with previous evidence that CDPPB is an agonist-PAM[8]. This peak at 0.9 is stabilized further when G_q is added to mGlu5 bound to CDPPB and Quis (fully active, Fig. 1a) (Fig. 4c,d, dark green). Although G_q can interact with both the intermediate 2a (FRET approximately 0.6) and intermediate 3a (FRET approximately 0.75) states, this 0.9 high-FRET, fully active state is likely to be a conformation of mGlu5 stabilized only in the presence of G protein (Fig. 4b,c; example traces are shown in Extended Data Fig. 12d). Although the structure of mGlu5-G_q has not been reported, structures of mGlu2 have been determined in the presence and absence of G protein, and no difference is observed between these mGlu2 structures[12,20]. However, our smFRET data show that, at least for mGlu5, there exists a distinct conformation in the presence of G protein.

Discussion

A long-standing interest in the Family C GPCR field is to understand how the signal to activate is allosterically communicated over a distance of 120 Å from the orthosteric agonist binding site to the TMD, which contains both the allosteric ligand binding pocket and the G protein

binding site. Using cryo-EM and smFRET data, we propose an activation model of mGlu5 and illustrate the effects of agonist, PAM and G protein on the functional states that range from inactive to fully active through several intermediates. Owing to intrinsic differences in the techniques, the conformational dynamics revealed by cryo-EM and smFRET are similar but not identical. However, the power of the comparison comes from observing the trends and the conformational relationships revealed by these complimentary methods, showing how ligands progressively advance the receptor dimer from inactive to active through intermediates.

Upon agonist binding, the upper lobes of the VFT close, whereas the lower lobes, CRDs and TMDs remain separated (intermediate 1a, Fig. 1a) (Figs. 2a and 4b). This Quis-bound intermediate 1a conformation in mGlu5 is different from the previously observed/proposed intermediate state in other mGlus, in which the agonist is bound to only one of the protomers[7,28]. The Quis-bound mGlu5 intermediate 1a is in equilibrium with the Quis-bound intermediate 2a (Fig. 1a) conformation, with the lower lobes of the VFT, CRDs and TMDs in proximity[2] (Figs. 2c and 4b). The addition of CDPPB results in asymmetric binding in the presence of Quis (in contrast to the symmetric binding seen in the absence of agonists) and further stabilizes an active conformation of mGlu5 (intermediate 3a, Fig. 1a) (Figs. 3a and 4b). Structurally, intermediate 3a resembles the intermediate 2a state (Fig. 3b), except in the conformation of ICL2 (Fig. 3d). Also, in the presence of Quis and CDPPB, there is evidence for a conformation of mGlu5 with reduced intersubunit distance, intermediate 3b (Figs. 1a and 4b). The addition of G protein stabilizes a unique signalling conformation as seen from the smFRET data (fully active, Fig. 1a) (Fig. 4b). The transition distributions in the transition density plot are symmetrically mirrored and are close to the diagonal axis, indicating the observed transitions happen step-wise (Extended Data Fig. 13). Only in the presence of CDPPB do we observe an off-diagonal peak. This might explain the ability of CDPPB as a PAM to lower the energy of the conformational transition to the active state (Extended Data Fig. 13).

Previously, smFRET studies have been carried out on CRD-labelled mGlu2 within detergent micelles in the presence of only ligands (G protein was not used)[28,29]. These studies have shown that the activation of mGlu2 with ligands occurs by transitioning through four states, and the addition of the PAM does not stabilize a new state but rather increases the occupancy of the active states. Similarly, in mGlu5, CDPPB alone and agonist alone do not seem to stabilize different states (Extended Data Fig. 12c). However, unlike with mGlu2, PAM addition to agonist-bound mGlu5 stabilizes a state not seen with agonist alone (intermediate 3a, Fig. 1a) (Fig. 4b). Further, the presence of G protein stabilizes a unique state not seen with ligands alone (fully active, Fig. 1a) (Fig. 4b), which is yet to be observed structurally. This perhaps indicates slightly different activation intermediates/pathways between different mGlu receptors.

In conclusion, the combined structural and dynamic data highlight the allosteric nature of mGlu5 activation, shedding light on the conformational diversity in receptor activation and its interactions with the G protein.

Online content

Any methods, additional references, Nature Portfolio reporting summaries, source data, extended data, supplementary information, acknowledgements, peer review information; details of author contributions and competing interests; and statements of data and code availability are available at https://doi.org/10.1038/s41586-024-07327-x.

1. Pin, J.-P. & Bettler, B. Organization and functions of mGlu and GABAB receptor complexes. *Nature* **540**, 60–68 (2016).
2. Koehl, A. et al. Structural insights into the activation of metabotropic glutamate receptors. *Nature* **566**, 79–84 (2019).
3. Moustaine, D. E. et al. Distinct roles of metabotropic glutamate receptor dimerization in agonist activation and G-protein coupling. *Proc. Natl Acad. Sci. USA* **109**, 16342–16347 (2012).
4. Gasparini, F. & Spooren, W. Allosteric modulators for mGlu receptors. *Curr. Neuropharmacol.* **5**, 187–194 (2007).
5. Ritchie, T. K. et al. Chapter 11 – Reconstitution of membrane proteins in phospholipid bilayer nanodiscs. *Methods Enzymol.* **464**, 211–231 (2009).
6. Nasrallah, C. et al. Direct coupling of detergent purified human mGlu5 receptor to the heterotrimeric G proteins Gq and Gs. *Sci. Rep.* **8**, 4407 (2018).
7. Seven, A. B. et al. G-protein activation by a metabotropic glutamate receptor. *Nature* **595**, 450–454 (2021).
8. Nasrallah, C. et al. Agonists and allosteric modulators promote signaling from different metabotropic glutamate receptor 5 conformations. *Cell Rep.* **36**, 109648 (2021).
9. Christopher, J. A., Doré, A. S. & Tehan, B. G. Potential for the rational design of allosteric modulators of class C GPCRs. *Curr. Top. Med. Chem.* **17**, 71–78 (2017).
10. Doré, A. S. et al. Structure of class C GPCR metabotropic glutamate receptor 5 transmembrane domain. *Nature* **511**, 557–562 (2014).
11. Christopher, J. A. et al. Structure-based optimization strategies for G protein-coupled receptor (GPCR) allosteric modulators: a case study from analyses of new metabotropic glutamate receptor 5 (mGlu5) X-ray structures. *J. Med. Chem.* **62**, 207–222 (2019).
12. Zhang, J. et al. Structural insights into the activation initiation of full-length mGlu1. *Protein Cell* **12**, 662–667 (2021).
13. Hlavackova, V. et al. Evidence for a single heptahelical domain being turned on upon activation of a dimeric GPCR. *EMBO J.* **24**, 499–509 (2005).
14. Fang, W. et al. Structural basis of the activation of metabotropic glutamate receptor 3. *Cell Res.* **32**, 695–698 (2022).
15. Goudet, C. et al. Asymmetric functioning of dimeric metabotropic glutamate receptors disclosed by positive allosteric modulators. *J. Biol. Chem.* **280**, 24380–24385 (2005).
16. Isberg, V. et al. Generic GPCR residue numbers – aligning topology maps while minding the gaps. *Trends Pharmacol. Sci.* **36**, 22–31 (2015).
17. Mølck, C. et al. Pharmacological characterization and modeling of the binding sites of novel 1,3-bis(pyridinylethynyl)benzenes as metabotropic glutamate receptor 5-selective negative allosteric modulators. *Mol. Pharmacol.* **82**, 929–937 (2012).
18. Gregory, K. J. et al. Probing the metabotropic glutamate receptor 5 ($mGlu_5$) positive allosteric modulator (PAM) binding pocket: discovery of point mutations that engender a "molecular switch" in PAM pharmacology. *Mol. Pharmacol.* **83**, 991–1006 (2013).
19. Gregory, K. J. et al. Identification of specific ligand-receptor interactions that govern binding and cooperativity of diverse modulators to a common metabotropic glutamate receptor 5 allosteric site. *ACS Chem. Neurosci.* **5**, 282–295 (2014).
20. Gregory, K. J. & Conn, P. J. Molecular insights into metabotropic glutamate receptor allosteric modulation. *Mol. Pharmacol.* **88**, 188–202 (2015).
21. Hellyer, S. D. et al. Probe dependence and biased potentiation of metabotropic glutamate receptor 5 is mediated by differential ligand interactions in the common allosteric binding site. *Biochem. Pharmacol.* **177**, 114013 (2020).
22. Dalton, J. A. R. et al. Shining light on an mGlu5 photoswitchable NAM: a theoretical perspective. *Curr. Neuropharmacol.* **14**, 441–454 (2016).
23. Punjani, A. & Fleet, D. J. 3D variability analysis: resolving continuous flexibility and discrete heterogeneity from single particle cryo-EM. *J. Struct. Biol.* **213**, 107702 (2021).
24. Punjani, A. & Fleet, D. J. 3DFlex: determining structure and motion of flexible proteins from cryo-EM. *Nat. Methods* **6**, 860–870 (2023).
25. Lin, S. et al. Structures of Gi-bound metabotropic glutamate receptors mGlu2 and mGlu4. *Nature* **594**, 583–588 (2021).
26. Brunette, A. M. J. & Farrens, D. L. Distance mapping in proteins using fluorescence spectroscopy: tyrosine, like tryptophan, quenches bimane fluorescence in a distance-dependent manner. *Biochemistry* **53**, 6290–6301 (2014).
27. Mansoor, S. E., Dewitt, M. A. & Farrens, D. L. Distance mapping in proteins using fluorescence spectroscopy: the tryptophan-induced quenching (TrIQ) method. *Biochemistry* **49**, 9722–9731 (2010).
28. Liauw, B. W.-H., Afsari, H. S. & Vafabakhsh, R. Conformational rearrangement during activation of a metabotropic glutamate receptor. *Nat. Chem. Biol.* **17**, 291–297 (2021).
29. Liauw, B. W.-H. et al. Conformational fingerprinting of allosteric modulators in metabotropic glutamate receptor 2. *eLife* **11**, e78982 (2022).
30. Vafabakhsh, R., Levitz, J. & Isacoff, E. Y. Conformational dynamics of a class C G-protein-coupled receptor. *Nature* **524**, 497–501 (2015).

Methods

mGlu5 purification

mGlu5 purification was carried out as previously described[2]. Briefly, human mGlu5 (21–872) with the haemagglutinin signal peptide, followed by a FLAG epitope tag (DYKDDDD) in the N terminus and a hexahistidine tag at the C terminus, was expressed in Sf9 cells using the Bac-to-Bac baculovirus expression system (Invitrogen). Sf9 cells at density a of 3.5×10^6 cells per ml were infected with mGlu5 virus grown for 48 h at 27 °C. Cells were collected by centrifugation and lysed in a hypotonic buffer containing 10 mM Tris at pH 7.8 and 1 mM EDTA with protease inhibitors. After centrifugation, the pellet was solubilized with 1% (w/v) *n*-dodecyl-β-D-maltoside (DDM) (Anatrace), 0.1% (w/v) cholesteryl hemisuccinate (CHS) (Steraloids), 0.2% (w/v) sodium cholate (Anatrace), 20 mM HEPES pH 7.5, 750 mM NaCl, 30% glycerol, iodoacetimide 2 mg ml^{-1}, protease inhibitor and 10 μM MTEP for 1.5 h at 4 °C. Ca^{2+} (5 mM) was added and the supernatant after centrifugation was incubated with anti-Flag M1 affinity resin for 2 h at 4 °C. The resin was washed with 0.1% (w/v) DDM, 0.01% (w/v) CHS, 500 mM NaCl, 20 mM HEPES pH 7.5, 2 mM Ca^{2+}, 10 μM MTEP, followed by 0.1% (w/v) DDM, 0.01% (w/v) CHS, 100 mM NaCl, HEPES pH 7.5, 2 mM Ca^{2+} and 10 μM MTEP. To exchange detergent to GDN, the column was washed with an increasing concentration of GDN and a decreased concentration of DDM. Finally, the column was washed with 0.2% (w/v) GDN, 0.002% (w/v) CHS, 100 mM NaCl, HEPES pH 7.5, 2 mM Ca^{2+} and 10 nM MTEP. The protein was eluted in 20 mM HEPES pH 7.5, 100 mM NaCl, 0.2% (w/v) GDN, 0.002%(w/v) CHS, 200 μg ml^{-1} Flag peptide, 5 mM EDTA and 10 nM MTEP. The eluted protein was concentrated in a 50 kDa cut-off Vivaspin (Millipore) and run on a Superose 6 size exclusion column (GE Healthcare) in 20 mM HEPES pH 7.5, 100 mM NaCl, 0.2% (w/v) GDN, 0.002% (w/v) CHS and 10 nM MTEP. Fractions containing mGlu5 were concentrated, flash-frozen and stored at −80 °C.

Purification of Nb43

Nb43 was purified as described previously[2]. Nb43 in a modified pE-SUMO vector with a PelB leader sequence and SUMO fusion tag was transformed into BL21 *Escherichia coli*, grown to an optical density at 600 nm of about 0.6 at 37 °C and induced with 1 mM IPTG. The flasks were transferred to 25 °C and allowed to express overnight (about 12 h). Bacteria were collected and Nb43 was purified from the periplasm. Cells were thawed with SET buffer (0.5 M sucrose, 0.5 mM EDTA and 0.2 M Tris pH 8.0) and stirred until homogenized. This was followed by the addition of three volumes of room temperature milli-Q water with rapid stirring for 45 min to release the periplasmic contents. Centrifugation was performed to remove cell debris and the supernatant, after the addition of 100 mM NaCl and 10 mM $MgCl_2$, was loaded onto an Ni-NTA resin. The resin was washed with 500 mM NaCl, 20 mM HEPES pH 7.5 and 20 mM imidazole, followed by 100 mM NaCl, 20 mM HEPES pH 7.5 and 20 mM imidazole. The SUMO-Nb43 was eluted in 100 mM NaCl, 20 mM HEPES pH 7.5 and 250 mM imidazole, and the His-SUMO tag was removed by the addition of ULP1. Protein was dialysed overnight into 100 mM NaCl and 20 mM HEPES pH 7.5 at 4 °C. Reverse Ni was performed to remove contaminants and uncleaved protein. Finally, Nb43 was subjected to size exclusion chromatography on a Superdex 200 10/30 column in 100 mM NaCl and 20 mM HEPES pH 7.5. Monomeric fractions were pooled, concentrated and flash-frozen in liquid nitrogen.

Nanodisc incorporation

mGlu5 in GDN was incorporated into MSP2N2 discs using the following ratio: 0.2 receptor:1 MSP2N2:120 POPC/POPG (3 POPC:2 POPG ratio). After 2 h of incubation on ice, biobeads were added at a ratio of 1:8 mg biobeads:lipids and incubated with shaking at 4 °C for 2 h. The same amount of biobeads was added again and further incubated with shaking at 4 °C overnight. The reconstitution mixture was separated from beads and applied on an M1-anti-FLAG column. After washing with 100 mM NaCl, 20 mM HEPES pH 7.5 and 15 mM Ca^{2+} to remove empty discs, the reconstituted protein was eluted in 100 mM NaCl, 20 mM HEPES pH 7.5, 200 μg ml^{-1} Flag peptide and 5 mM EDTA. Nanodisc-incorporated mGlu5 was concentrated and injected on a Superose 6 10/30 gel filtration column in 100 mM NaCl, 20 mM HEPES pH 7.5. Monomeric peak fractions were collected and concentrated to about 5 mg ml^{-1} for imaging.

G protein purification

Heterotrimeric G protein (G_q) was purified as previously described[31]. *Trichoplusia ni* (Hi5) cells (Expression Systems) were co-infected with three viruses, one encoding wild-type human $G\alpha_q$; another encoding wild-type human β1γ2, with an 8 × His tag on the β1 subunit with HRV-3C protease cleavable site; and a the third virus encoding Ric8A. Cells were collected at 48 h post-infection and lysed in hypotonic buffer. The pellet was solubilized in buffer containing 1% sodium cholate (Sigma Aldrich) and 0.05% DDM. The lysate was purified with Ni-chelating sepharose chromatography, and the detergent was exchanged from cholate/DDM mixture to DDM alone. The eluted protein was dialysed against a buffer containing 20 mM HEPES pH 7.5, 100 mM NaCl, 1 mM $MgCl_2$, 0.05% DDM, 100 μM Tris(2-carboxyethyl)phosphine hydrochloride (TCEP) (Sigma Aldrich) and 10 μM GDP (Sigma Aldrich) in the presence of HRV-3C protease. Reverse Ni chromatography was performed to further purify the protein. The flowthrough from the Ni column was subjected to the MonoQ 10/100 GL column (GE Healthcare). Protein was bound to the column and washed in buffer A (20 mM HEPES pH 7.5, 50 mM sodium chloride, 1 mM magnesium chloride, 0.05% DDM, 100 μM TCEP and 10 μM GDP). The protein was eluted with a linear gradient of 0–50% buffer B (buffer A with 1 M NaCl). The collected G protein was dialysed into 20 mM HEPES pH 7.5, 100 mM sodium chloride, 1 mM magnesium chloride, 0.02% DDM, 100 μM TCEP and 10 μM GDP. Protein was concentrated to 250 μM and flash-frozen until further use.

GTP turnover assay

Analysis of GTP turnover was performed by using a modified protocol of the GTPase-Glo assay (Promega) described previously[32]. In the presence (20 μM) or absence of ligand, mGlu5 (1 μM in GDN and 0.5 μM in nanodisc) and G_q (1 μM for mGlu5 in GDN and 0.5 μM for mGlu5 in Nanodisc) were mixed in 20 mM HEPES pH 7.5, 50 mM NaCl, 0.01% GDN/0.001% CHS (or no detergent for nanodisc sample), 100 μM TCEP, 10 μM GDP and 10 μM GTP, and incubated at room temperature for 120 min. GTPase-Glo reagent was added to the sample and incubated for 30 min. Luminescence was measured after the addition of detection reagent and incubation for 10 min at room temperature using a SpectraMax Paradigm plate reader.

HDX-MS

Hydrogen–deuterium exchange labelling reaction. Purified mGlu5 at 60 μM [monomer] was diluted to 20 μM [monomer] in 100 mM NaCl, 20 mM HEPES, 0.05% GDN/0.005% CHS to match the concentration of mGlu5 in nanodisc (also 20 μM [monomer]). Subsequently, mGlu5 in detergent was further diluted 1:1 to 10 μM [monomer] with 10 mM monosodium glutamate, 100 mM NaCl, 20 mM HEPES, 0.05% GDN/0.005% CHS, pH 7.5, such that the final concentration of glutamate in this sample was 5 mM. An equivalent mGlu5 sample in detergent was also prepared in the absence of glutamate. Similarly, mGlu5 in nanodiscs was diluted 1:1 to 10 μM [monomer] with 10 mM monosodium glutamate, 100 mM NaCl, 20 mM HEPES pH 7.5. All samples were incubated for 30 min at room temperature.

To prepare deuterated buffer, 5 ml of 10× buffer of 1 M NaCl, 200 mM HEPES, with or without 100 mM monosodium glutamate, at pH 7.5 was lyophilized overnight and then resuspended in D_2O. The 1× buffers were prepared by a 1:9 dilution with D_2O, and a buffer of 5 mM monosodium glutamate was prepared by combining those same buffers in a 1:1 ratio. To prepare quench buffer, 27 mg of zirconium (IV) oxide, used for lipid

extraction, was combined with 1 ml of quench buffer (3 M urea, 20 mM TCEP, pH 2.4), vortexed and left on ice.

To initiate exchange, samples were diluted 1:10 into D_2O buffer and quenched 1:1 with cold quench buffer for a total sample volume of 80 µl and left on ice. At each time point, 0.8 µl of porcine pepsin (10 mg ml^{-1}; Sigma Aldrich) and 0.8 µl of aspergillopepsin (10 mg ml^{-1}; Sigma Aldrich) were added to each sample, then rapidly vortexed and returned to ice for 3.5 min. Next, 0.8 µl of Nepenthesin II (10 mg ml^{-1}; AffiPro) was added in two of the three HDX-MS replicates, which gave only marginal improvement in peptide coverage; we report peptide uptake plots only for peptides found in all three replicates. To remove zirconium (IV) oxide, each sample was transferred to a temperature-controlled centrifuge and spun up to maximum speed (21.1*g*); the supernatant was then transferred to a new tube and flash-frozen in liquid N_2. Samples were stored at −80 °C before liquid chromatography/mass spectrometry (LC/MS) analysis. Proteases were resuspended in 100 mM NaCl, 20 mM HEPES, pH 7.5 to 10 mg ml^{-1}, and filtered (0.22 µm filter, Corning), aliquoted, flash-frozen and stored at −80 °C before use.

Liquid chromatography/mass spectrometry analysis. Samples were thawed and injected into a cooled valve system (Trajan LEAP) coupled to a liquid chromatography system (Thermo Ultimate 3000) flowing buffer A (0.1% formic acid) at 200 µl min^{-1}. The valve chamber, trap column and analytical column were kept at 2 °C.

Peptides were desalted for 4 min on a trap column (1 mM ID × 2 cm, IDEx C-128) manually packed with POROS R2 reversed-phase resin (Thermo Scientific). Peptides were then separated on a C18 analytical column (Waters Acquity UPLC BEH C18 Column, pore size 130 Å, particle size 1.7 µm, 2.1 mm ID × 50 mm) with buffer B (100% acetonitrile, 0.1% formic acid) flowing at a rate of 40 µl min^{-1}, increasing from 5% to 40% over the first 14 min and from 40% to 90% B over 30 s, and dropping to 5% B after 2.5 min. After 30 s, two sawtooth gradients (5% to 40% B over 30 s, 40% to 90% B over 30 s, hold at 90% B for 30 s, drop to 5% B over 30 s, hold at 5% B for 30 s) were performed. Peptides were eluted into a Q Exactive Orbitrap mass spectrometer (Thermo Fisher) operating in positive ion mode (MS1 settings: resolution 140,000, AGC target 3×10^6, maximum IT 200 ms, scan range 300–1500 m/z). For tandem mass spectrometry, mGlu5 samples were analysed using the MS1 settings described above, with resolution 70,000, and MS2 settings as follows: resolution 17,500, AGC target 2×10^5, maximum IT 100 ms, loop count 10, isolation window 2.0 m/z, NCE 28, charge states 1 and >8 excluded, dynamic exclusion 15.0 s.

Sample time points were injected in non-consecutive order, and, after every injection, a shortened, blank injection was performed to monitor for protein carryover. Briefly, blank runs were carried out with buffer A flowing at 300 µl min^{-1}. Any remaining material within the sample loop, as well as wash buffer, was desalted for 2 min on the same trap column; the remaining material was then separated on the same C18 analytical column flowing at a rate of 40 µl min^{-1}, increasing from 5% to 40% over the first 1.5 min and from 40% to 90% B over 30 s, and dropping to 5% B after 30 s. After 30 s of holding at 5% B, two sawtooth gradients (5% to 40% B over 30 s, 40% to 90% B over 30 s, hold at 90% B for 30 s, drop to 5% B over 30 s, hold at 5% B for 30 s) were then performed.

Peptide identification and analysis. MS2 data were processed using Byonic (Protein Metrics), resulting in a reference list of peptides, including several peptides containing glycosylation sites. Hydrogen–deuterium exchange data were analysed in HD-Examiner (v.3.1) using default settings, and uptake values were adjusted to reflect that the final samples were 90% deuterated. Where necessary, peptide retention time histograms were manually adjusted to ensure consistency across all time points. Uptake summary data were exported from HD-Examiner and used to create uptake curves and Woods plots using Python scripts. A difference in deuteration of less than 10% between the two conditions was not considered significant, as indicated by horizontal dashed lines on Woods plots.

Cryo-EM

Sample preparation and data acquisition. mGlu5 in nanodiscs was incubated with Quis alone (and Nb43), Quis and CDPPB (G_qiN and Nb43), or CDPPB alone for 2 h at room temperature. For grid preparation, 3 µl of purified mGlu5 (with the different ligands) at 5 mg ml^{-1} was applied on glow-discharged holey carbon gold grids (Quantifoil R1.2/1.3, 200 mesh). The grids were blotted using a Vitrobot Mark IV (FEI) with 3 s blotting time and blot force 3 at 4 °C and 100% humidity and plunge-frozen in liquid ethane.

Image processing and three-dimensional reconstructions. For all three samples, namely CDPPB-bound mGlu5, Quis- and Nb43-bound mGlu5, and Quis + CDPPB-bound mGlu5, cryo-EM data were collected on a Titan Krios electron microscope operating at 300 kV and equipped with a K3 direct electron detector. Videos were acquired in counting mode with a calibrated pixel size of 1.111 Å per pixel and a total dose of approximately 51.6 electrons per Å^2, fractionated across 50 frames (Extended Data Figs. 3, 5 and 6 and Extended Data Table 1).

Single-particle data processing was performed using cryoSPARC 3.3.2 (ref. 33). Initially, motion correction and contrast transfer function (CTF) estimation were carried out using Patch Motion Corr and Patch CTF, followed by template-based particle picking using previously determined mGlu5 structures (EMD-0345 or EMD-0346). The detailed data processing workflows can be found in Extended Data Figs. 3, 5 and 6. Picked particles were sorted using 2D classification, ab initio, and heterogenous refinement. For each structure/conformation, we applied both global non-uniform refinement[34] and local refinement on the CRD–TMD region. The final maps, generated with UCSFChimera[35], are composite maps of the global non-uniform refinement and the locally refined CRD–TMD region. Map sharpening was performed with Autosharpen within Phenix[36,37].

Lastly, local resolution estimation and 3D Fourier shell correlation (FSC) were employed to assess the local resolution and orientation distribution of the final dataset[38].

Model building and refinement. The initial template was mGlu5 from PDB codes 6N51 and 6N52. Ligand coordinates and geometry restraints were generated using phenix.elbow[36]. Coot[39] was used for iterative model building and the final model was subjected to global refinement and minimization in real space using phenix.real_space_refine in Phenix[36]. FSC curves were calculated between the resulting model and the half map used for refinement as well as between the resulting model and the other half map for cross-validation (Extended Data Figs. 3, 5 and 6). The final refinement parameters are provided in Extended Data Table 1.

Molecular dynamics simulations

System setup. Simulation systems were built with CHARMM-GUI[40] using the Membrane Builder[41]. The monomer of the TMD for the receptor in complex with CDPPB (CDPPB-bound mGluR5 intermediate 1b, residues 567–673 and 687–827) was selected. CHARMM General Force Field[42] was used to generate topology and parameter files for CDPPB. Missing side chains were modelled in Maestro using the protein preparation wizard[43]. Titratable groups were simulated in their dominant protonation state for pH 7. The receptors were placed in the membrane by aligning the first principal axis, followed by visual inspection. The aligned structures were then inserted into a POPC bilayer with a minimum water height on either side of the bilayer of 22.5 Å and a bilayer area chosen to be about four times that of the protein surface, normalizing the upper and lower leaflet surface area by further POPC molecules accordingly. Then, 150 mM potassium chloride (KCl) ions were added to neutralize the system charge.

Simulation protocol. All simulations were performed with the CHARM-M36m force field for proteins, ions and lipids, and the TIP3 model was used for waters[44,45]. Simulations were performed using OpenMM[46]. The system was equilibrated initially with 1 fs time steps (125 ps per run for three runs) followed by 2 fs time steps (500 ps per run for three runs) for a total of six equilibration steps each with continually decreasing force constants applied to the protein backbone (10.0, 5.0, 2.5, 1.0, 0.5, 0.1 kcal mol^{-1} $Å^{-2}$), side chains (5.0, 2.5, 1.0, 0.5, 0.1, 0.0 kcal mol^{-1} $Å^{-2}$), waters and lipids (2.5, 2.5, 1.0, 0.5, 0.1, 0.0 kcal mol^{-1} $Å^{-2}$), and ions (10.0, 0.0, 0.0, 0.0, 0.0, 0.0 kcal mol^{-1} $Å^{-2}$). Production runs were performed in NPT ensemble at 310.15 °K at 1 bar with 4 fs time steps, employing hydrogen mass repartitioning[47]. A switching distance of 10 Å and cut-off distance of 12 Å were used for non-bonded interactions, and long-range electrostatics were computed with particle mesh Ewald. Coordinates were written out every 100 ps. The trajectory analyses were done using MDAnalysis[48].

3DVA and 3DFlex analysis of cryo-EM data. CryoSPARC's 3D Variability Analysis (3DVA) was used to investigate the conformational heterogeneity in the final datasets for Quis-bound or Quis + CDPPB-bound active state[23]. The particles used for final non-uniform refinement were processed by 3DVA with three modes and a mask encompassing the whole receptor, including the nanodisc. Following 3DVA, the three principal components were subjected to 3DVA Display using simple output mode and 20 frames. The resolution was low-pass filtered to 5 Å to avoid noise dominating the determination of eigenvectors. The results were visualized using UCSFChimera (Supplementary Video 1).

CryoSPARC's 3D Flexible Refinement (3DFlex) was also used to investigate and confirm the conformational heterogeneity in the Quis + CDPPB-bound active state[24]. For 3DFlex on the whole receptor, the particles used for the final non-uniform refinement were cropped into 256 pixels (1.48 Å per pixel) for reconstruction and 128 pixels (2.95 Å per pixel) for training. A mask, which encompassed the whole receptor including the nanodisc, was divided into 20 tetrahedral cells to prepare the mesh. For 3DFlex training, we optimized different parameters and ended up using three latent dimensions, 0.1 rigidity prior strength and 10 latent centring strength. The latent distributions along three dimensions are visualized using UCSFChimera (Supplementary Video 2).

For 3DFlex on the CRD + TM regions, the particles used for TM local refinement were kept in their original box size for data preparation and cropped into 170 pixels (2.22 Å per pixel) for training. A mask encompassing the TM regions (Extended Data Fig. 5a), excluding the nanodisc, was divided into 40 tetrahedral cells to prepare the mesh. For 3DFlex training, we optimized different parameters and ended up using three latent dimensions, 0.5 rigidity prior strength and 10 latent centring strength. The latent distributions along three dimensions are visualized using UCSFChimera (Supplementary Video 2).

Minimal cysteine expression and purification

We developed a minimal cysteine (minCys) construct of mGlu5 to enable site-specific labelling. In mGlu5, two Cys residues, one in the intracellular end of TM4 ($C691^{4.30}$) and the other in ICL2 ($C681^{ICL2}$), seem to be exposed to being labelled; mutation of these to Ala largely abolished background labelling. Human mGlu5 (21–872) with the haemagglutinin signal peptide, followed by a FLAG epitope tag (DYKDDDD) in the N terminus and a hexahistidine tag at the C terminus, was cloned into pcDNA-Zeo-tetO. Two native cysteine residues were mutated to make the minCys construct ($C691^{4.30}$A and $C681^{ICL2}$A) and for bimane spectroscopy studies a single $C691^{4.30}$A mutant was cloned. For smFRET studies, an engineered Cys was introduced into the CRD (at position 560). The bimane and smFRET constructs were transfected into Expi293F (Thermo Fisher) cells stably expressing the tetracycline repressor using an Expifectamine transfection kit (Thermo Fisher) following the manufacturer's recommendations, with the following modifications. At 2 days post-transfection, mGlu5 expression was induced with doxycycline (4 μg ml^{-1} and 5 mM sodium butyrate) in the presence of 1 μM MTEP. Cells were collected 30 h post-induction and stored at −80 °C until use. Further purification and nanodisc incorporation were performed following the protocol described earlier for pellets from insect cells.

Bimane spectroscopy

Wild-type mGlu5 or $C691^{4.30}$A mutant in nanodisc at 10 μM was incubated with a 10-molar excess of bimane at room temperature for 1 h. The excess label was removed using size exclusion chromatography on a Superose 6 10/300 Increase column in 20 mM HEPES pH 7.5 and 100 mM NaCl. Bimane-labelled mGlu5 at 0.1 μM was incubated with ligands (10 μM) for 1 h at room temperature. Fluorescence data were collected at room temperature in a 150 μl cuvette with FluorEssence v.3.8 software on a Fluorolog instrument (Horiba) in photon-counting mode. Bimane fluorescence was measured by excitation at 370 nm with excitation and emission bandwidth passes of 4 nm. The emission spectra were recorded from 410 to 510 nm with a 1 nm increment and 0.1 s integration time.

smFRET

Sample preparation and data collection. Nanodisc-incorporated minCys mGlu5 (with residues $C691^{4.30}$ and $C681^{ICL2}$ mutated) with an introduced Cys at position 560 was incubated with a 5-molar excess of donor (LD555) and a 10-molar excess of acceptor (LD655) at room temperature for 20 min. Following incubation with 5 mM cysteine for 10 min, the sample was subjected to size exclusion chromatography on a Superose 6 10/300 Increase column in 20 mM HEPES pH 7.5 and 100 mM NaCl, for the removal of excess labels.

mPEG (Lysan Bio) was used to passivate glass coverslips (VWR) and, further doped with biotin PEG16, to inhibit non-specific protein adsorption. The coverslips, before each experiment, were incubated with NeutrAvidin (Thermo Fisher), followed by 10 nM biotinylated antibody (mouse anti-FLAG, GenScript). Chambers were flushed to remove reagents between each conjugation step. The anti-FLAG antibody was diluted and washed in 50 mM NaCl, 10 mM Tris, pH 7.5. Labelled mGlu5 was diluted around 100-fold and applied to coverslips to achieve optimum surface immobilization (about 400 molecules in a 2,000 $μm^2$ imaging area). Unbound receptors were washed away with buffer. smFRET imaging was performed in an imaging buffer consisting of 3 mM Trolox, 100 mM NaCl, 2 mM $CaCl_2$, 20 mM HEPES pH 7.5 and an oxygen scavenging system (0.8% dextrose, 0.8 mg ml^{-1} glucose oxidase and 0.02 mg ml^{-1} catalase). Samples were imaged with a 1.49 NA ×60 objective (Olympus) on a total internal reflection fluorescence microscope with 100 ms resolution time unless stated otherwise. Lasers at 532 nm (Cobolt) and 633 nm (Melles Griot) were used for donor and acceptor excitation, respectively. Fluorescence was passed through a Chroma ET550lp filter and split into donor and acceptor signals with a Chroma T635lpxr. FRET efficiency was calculated as $(I_A - 0.1I_D)/(I_D + I_A)$, in which I_D and I_A are the donor and acceptor intensities, respectively, after background subtraction. Imaging was with 100 ms acquisition time (10 Hz) with a Photometrics Prime 95B CMOS camera.

smFRET data processing. The fluorescence videos were analysed with SPARTAN v.3.7 (ref. 49). Donor and acceptor channels were aligned using the first ten frames of each video while excluding particles closer than 3.5 pixels using an integration window of 12 pixels. Traces showing single-donor and single-acceptor photobleaching with a stable total intensity of longer than 5 s (50 frames), signal-to-noise ratio as defined by the background (SNRbg) greater than 15 and donor/acceptor correlation coefficients less than 0 were collected (20–30% of total molecules per imaging area). We included for analysis only traces that showed co-localization of one donor and one acceptor, as determined automatically by SPARTAN. A nonlinear filter[50] was used for smoothing individual traces with the following filter parameters: window = 2, M = 2

and P = 15 for histograms. smFRET histograms were compiled from 100 or more molecules per condition (100 ms time resolution). Error bars in the histograms represent s.e.m. from 4 or more independent videos. To ensure that traces of different lengths contributed equally, histograms from individual traces were normalized to one before compiling. Histograms were fit to three Gaussians (fit constraints are shown in Supplementary Table 1), on the basis of the Akaike information criterion (AIC) (Extended Data Fig. 12a). AIC is a statistical method used for model selection that tests how well the model fits the data without over-fitting. The AIC 'rewards' models that achieve high goodness-of-fit scores and penalizes overly complex models. By itself, the AIC score is less useful, but it becomes a powerful statistical method when used as a comparative tool for competing models. The model with the lowest AIC score strikes a superior balance between its ability to fit the data-set and its ability to avoid over-fitting. The corrected AIC (cAIC) was calculated using the in-built cAIC equation in GraphPad Prism 9. For the transition density plots, vbFRET software was used to fit raw FRET traces with a hidden Markov model[51]. Individual traces were fit with a maximum of five states and transition density plots were graphed with TDP plots script[52]. All traces from each condition dataset were included in generating hidden Markov models.

Reporting summary

Further information on research design is available in the Nature Portfolio Reporting Summary linked to this article.

Data availability

The data that support this study are available from the corresponding authors upon request. The cryo-EM density maps have been deposited in the Electron Microscopy Data Bank (EMDB) under accession codes EMD-41092, EMD-41099, EMD-41139 and EMD-41069. Model coordinates have been deposited in the Protein Data Bank (PDB) under accession numbers 8T7H, 8T8M, 8TAO and 8T6J. Previously published structures can be accessed via accession codes: 6N50, 6N51, 6N52, 7FD9, 6N4Y, 6FFI, 7MTR, 7MTS. EMBD codes of available structures mentioned in this manuscript: EMD-0345 or EMD-0346. Source data are provided with this paper.

31. Maeda, S. et al. Development of an antibody fragment that stabilizes GPCR/G-protein complexes. *Nat. Commun.* **9**, 3712 (2018).
32. Gregorio, G. G. et al. Single-molecule analysis of ligand efficacy in β_2AR-G-protein activation. *Nature* **547**, 68–73 (2017).
33. Punjani, A., Rubinstein, J. L., Fleet, D. J. & Brubaker, M. A. cryoSPARC: algorithms for rapid unsupervised cryo-EM structure determination. *Nat. Methods* **14**, 290–296 (2017).
34. Punjani, A., Zhang, H. & Fleet, D. J. Non-uniform refinement: adaptive regularization improves single-particle cryo-EM reconstruction. *Nat. Methods* **17**, 1214–1221 (2020).
35. Pettersen, E. F. et al. UCSF Chimera—a visualization system for exploratory research and analysis. *J. Comput. Chem.* **25**, 1605–1612 (2004).
36. Adams, P. D. et al. The Phenix software for automated determination of macromolecular structures. *Methods* **55**, 94–106 (2011).
37. Terwilliger, T. C., Sobolev, O. V., Afonine, P. V. & Adams, P. D. Automated map sharpening by maximization of detail and connectivity. *Acta Crystallogr. D Struct. Biol.* **74**, 545–559 (2018).
38. Tan, Y. Z. et al. Addressing preferred specimen orientation in single-particle cryo-EM through tilting. *Nat. Methods* **14**, 793–796 (2017).
39. Emsley, P., Lohkamp, B., Scott, W. G. & Cowtan, K. Features and development of Coot. *Acta Crystallogr. D Biol. Crystallogr.* **66**, 486–501 (2010).
40. Jo, S., Kim, T., Iyer, V. G. & Im, W. CHARMM-GUI: a web-based graphical user interface for CHARMM. *J. Comput. Chem.* **29**, 1859–1865 (2008).
41. Lee, J. et al. CHARMM-GUI membrane builder for complex biological membrane simulations with glycolipids and lipoglycans. *J. Chem. Theory Comput.* **15**, 775–786 (2019).
42. Vanommeslaeghe, K. et al. CHARMM general force field: a force field for drug-like molecules compatible with the CHARMM all-atom additive biological force fields. *J. Comput. Chem.* **31**, 671–690 (2010).
43. Sastry, G. M., Adzhigirey, M., Day, T., Annabhimoju, R. & Sherman, W. Protein and ligand preparation: parameters, protocols, and influence on virtual screening enrichments. *J. Comput. Aided Mol. Des.* **27**, 221–234 (2013).
44. Huang, J. et al. CHARMM36m: an improved force field for folded and intrinsically disordered proteins. *Nat. Methods* **14**, 71–73 (2017).
45. Jorgensen, W. L., Chandrasekhar, J., Madura, J. D., Impey, R. W. & Klein, M. L. Comparison of simple potential functions for simulating liquid water. *J. Chem. Phys.* **79**, 926–935 (1983).
46. Eastman, P. et al. OpenMM 7: rapid development of high performance algorithms for molecular dynamics. *PLoS Comput. Biol.* **13**, e1005659 (2017).
47. Gao, Y. et al. CHARMM-GUI supports hydrogen mass repartitioning and different protonation states of phosphates in lipopolysaccharides. *J. Chem. Inf. Model.* **61**, 831–839 (2021).
48. Michaud-Agrawal, N., Denning, E. J., Woolf, T. B. & Beckstein, O. MDAnalysis: a toolkit for the analysis of molecular dynamics simulations. *J. Comput. Chem.* **32**, 2319–2327 (2011).
49. Juette, M. F. et al. Single-molecule imaging of non-equilibrium molecular ensembles on the millisecond timescale. *Nat. Methods* **13**, 341–344 (2016).
50. Haran, G. Noise reduction in single-molecule fluorescence trajectories of folding proteins. *Chem. Phys.* **307**, 137–145 (2004).
51. Bronson, J. E., Fei, J., Hofman, J. M., Gonzalez, R. L. & Wiggins, C. H. Learning rates and states from biophysical time series: a Bayesian approach to model selection and single-molecule FRET data. *Biophys. J.* **97**, 3196–3205 (2009).
52. McKinney, S. A., Joo, C. & Ha, T. Analysis of single-molecule FRET trajectories using hidden Markov modeling. *Biophys. J.* **91**, 1941–1951 (2006).

Acknowledgements We thank D. Hilger for helpful discussions. The cryo-EM data were collected at Stanford Cryo-Electron Microscopy Center (cEMc). This work was supported by National Institutes of Health grants no. K99GM148823 (N.R.L.), no. R01NS119826 (E.Y.I.) and nos. R01NS028471 and R01NS122394 (B.K.K.). We thank the National Institute of Drug Abuse (NIDA). E.Y.I. is a Weill Neurohub Investigator. S.M. and B.K.K. are Chan Zuckerberg Biohub Investigators.

Author contributions K.K.K. and B.K.K. conceived the project. K.K.K. prepared samples, froze grids and collected cryo-EM data with help from C.Z. and E.M. K.K.K. and J.X. developed the minimal cysteine mGlu5 construct and performed bimane studies, and made smFRET samples with help from E.S.O. H.W. processed cryo-EM data, performed the 3DVA and 3DFlex analysis and performed molecular dynamics simulations. C.H. collected and analysed smFRET data under the supervision of E.Y.I. N.R.L. collected and analysed the HDX-MS data under the supervision of S.M. A.K. helped with structure analysis. K.K.K., H.W. and B.K.K. wrote the manuscript with input from all authors.

Competing interests B.K.K. is co-founder of and consultant for ConfometRx. The remaining authors declare no competing interests.

Additional information

Supplementary information The online version contains supplementary material available at https://doi.org/10.1038/s41586-024-07327-x.

Correspondence and requests for materials should be addressed to Kaavya Krishna Kumar or Brian K. Kobilka.

Peer review information *Nature* thanks Karen Gregory, David Millar and Ryoji Suno for their contribution to the peer review of this work. Peer reviewer reports are available.

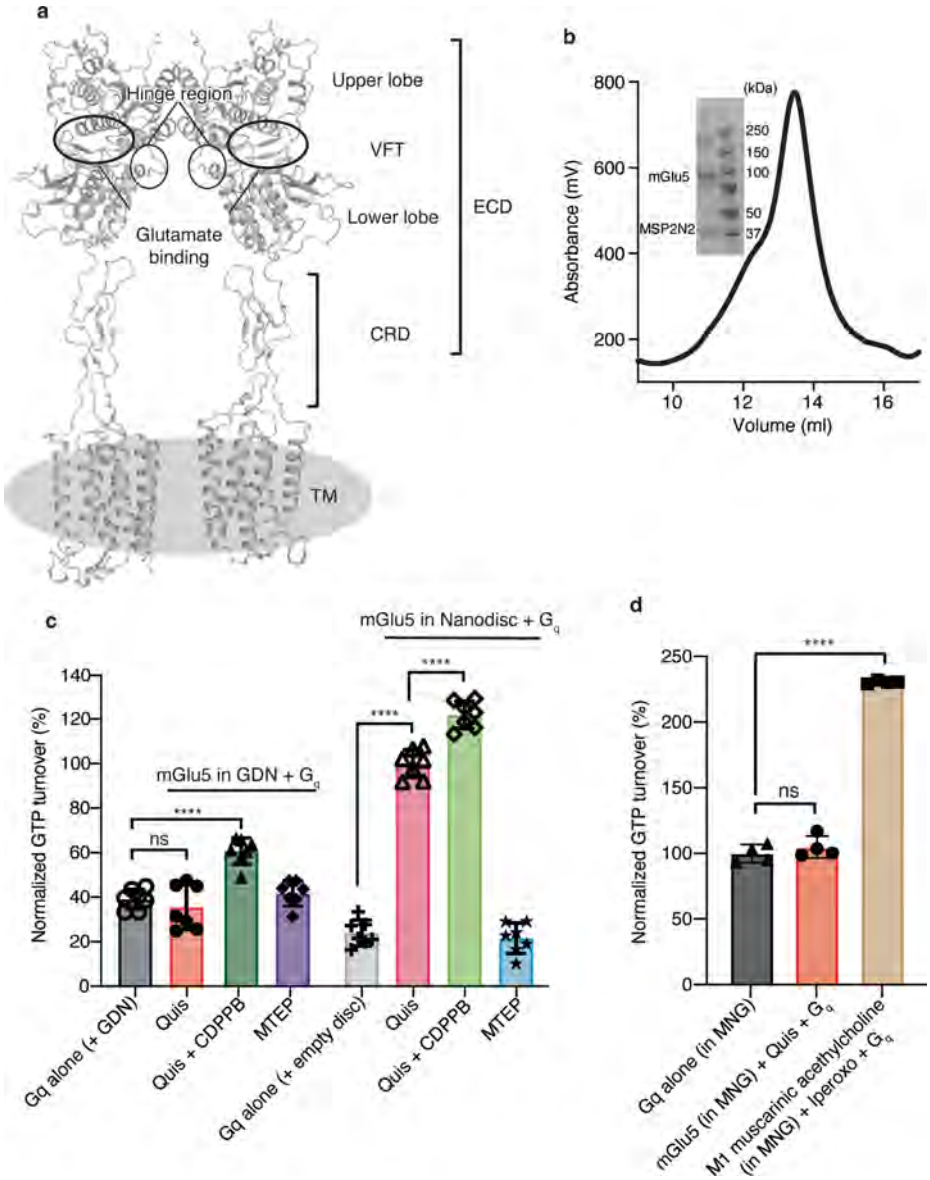

Extended Data Fig. 1 | mGlu5 activation in detergent compared to lipid environment. (a) Structural domains of mGlu5. (b) Representative size exclusion chromatography trace and SDS-PAGE gel (for gel source data, see Supplementary Fig. 1a) of mGlu5 in nanodisc (n = 6). (c) GTP turnover assay showing mGlu5 induced G_q turnover. In the presence of agonist Quis (20 μM), mGlu5 in detergent does not induce significant G_q (red) turnover compared to G_q alone (grey). The addition of Quis and CDPPB (20 μM) (dark green) to mGlu5 in detergent results in a small but significant increase in G protein turnover. With mGlu5 in nanodiscs, the addition of Quis significantly increases G_q turnover (magenta). Quis and CDPPB (light green) further increase the GTP turnover of G_q. The negative allosteric modulator, MTEP inhibits turnover in mGlu5 nanodiscs condition (blue). Data represented as mean ± s.d., ns= 0.4124, $p < 0.0001$****, unpaired *t*-test (two-tailed) performed for statistical analysis between two conditions. One-way ANOVA performed for comparison across multiple conditions showed p < 0.0001. n = 7 individual experiments (data normalization was done with the average value of Quis-bound mGlu5 in nanodiscs as 100% and receptor alone as 0%). (d) In the presence of the agonist iperoxo, muscarinic acetylcholine M1 receptor (in MNG) induces significant GTP turnover in G_q ($p < 0.0001$****). But no difference is seen with Quis-bound mGlu5 (in MNG) and G_q (ns = 0.5374). Data represented as mean ± s.d., *p* values are from unpaired *t*-test (two-tailed) performed for statistical analysis between two conditions. One-way ANOVA performed for comparison across multiple conditions showed p < 0.0001. n = 4 individual experiments. Data normalization was done with the average value of G_q in MNG as 100% and buffer alone as 0%.

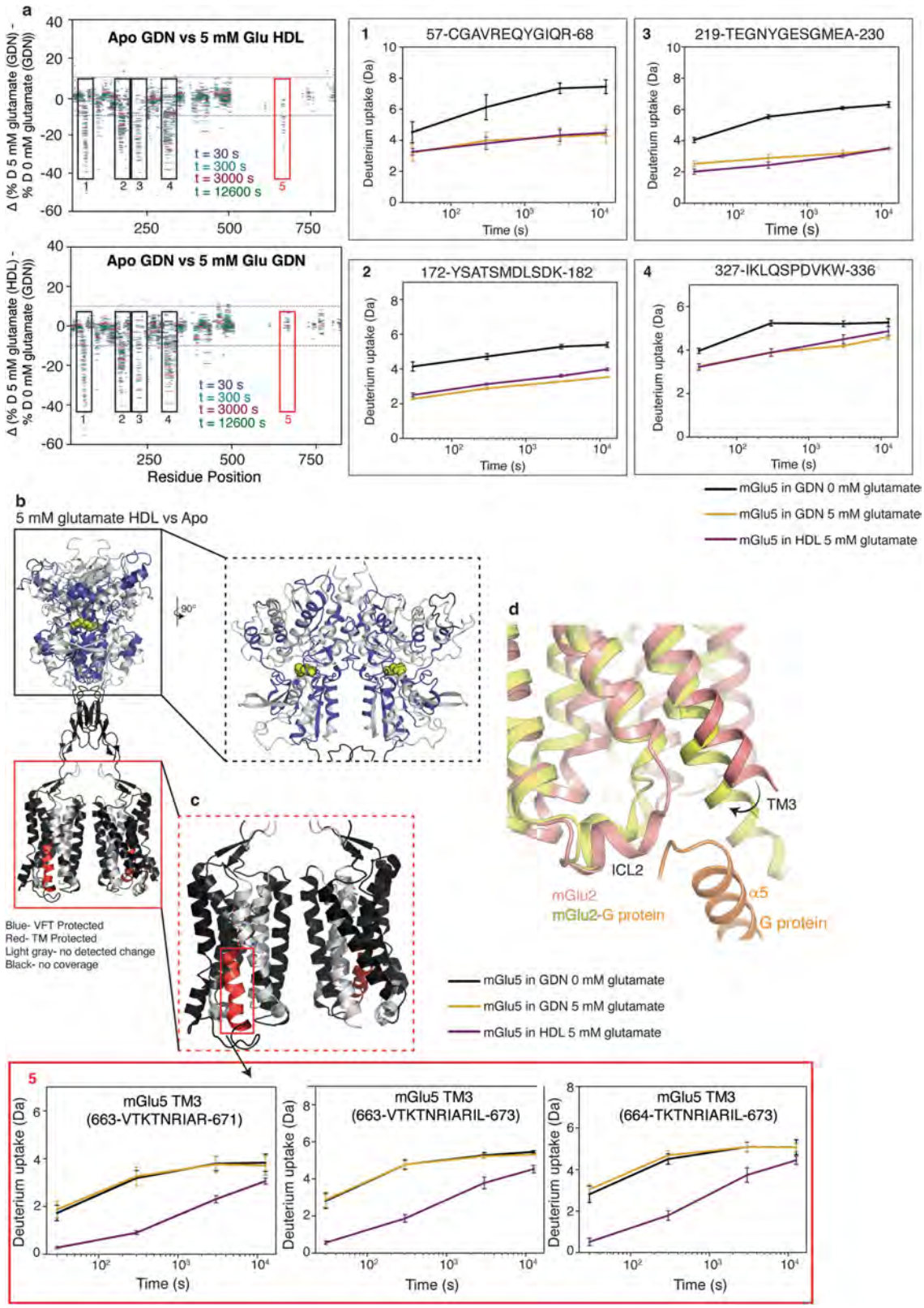

Extended Data Fig. 2 | See next page for caption.

Extended Data Fig. 2 | HDX-MS of mGlu5 in detergent and nanodisc. (a) HDX-MS data are shown as Woods plots, i.e., as the difference in the percent deuteration for a given peptide at a given time point against the sequence position for Apo mGlu5 in detergent (GDN) vs 5 mM glutamate-bound mGlu5 in detergent (GDN) (top) and Apo mGlu5 in detergent (GDN) vs 5 mM glutamate-bound mGlu5 in nanodisc (HDL) (bottom). Black boxes numbered 1- 4 are example regions in the VFT that show differences in deuterium uptake between the Apo and 5 mM glutamate conditions, regardless of the membrane environment, but no detectable difference between mGlu5 in detergent (GDN) and nanodisc (HDL) in the presence of 5 mM glutamate (the corresponding deuterium uptake plots are shown on the right). The red box is a region in the TM that shows a difference between agonist-bound mGlu5 in detergent and nanodisc (HDX-MS exchange curves shown in Extended Data Fig. 2c). All measurements done in triplicates, data represented at mean ± s.e.m. Woods plots are shown for a single replicate. (b) HDX-MS changes in Apo mGlu5 in detergent and agonist-bound mGlu5 in nanodisc are plotted onto the mGlu5 structure (PDB code: 6N51). (c) The region of TM3 where peptides were observed in HDX-MS measurements is shown in red. Deuterium uptake plots of these TM3 peptides (n = 3, red box) show that receptor in GDN under the Apo condition (black) and in the presence of 5 mM glutamate (yellow) overlay well, whereas TM3 peptides of mGlu5 in nanodisc in the presence of 5 mM glutamate (magenta) exhibit reduced uptake relative to both GDN conditions. (d) Agonist-bound mGlu2 (PDB code: 7MTR) is overlayed with agonist-bound mGlu2-G protein complex (PDB code: 7MTS) showing conformational changes in the intracellular region of TM3.

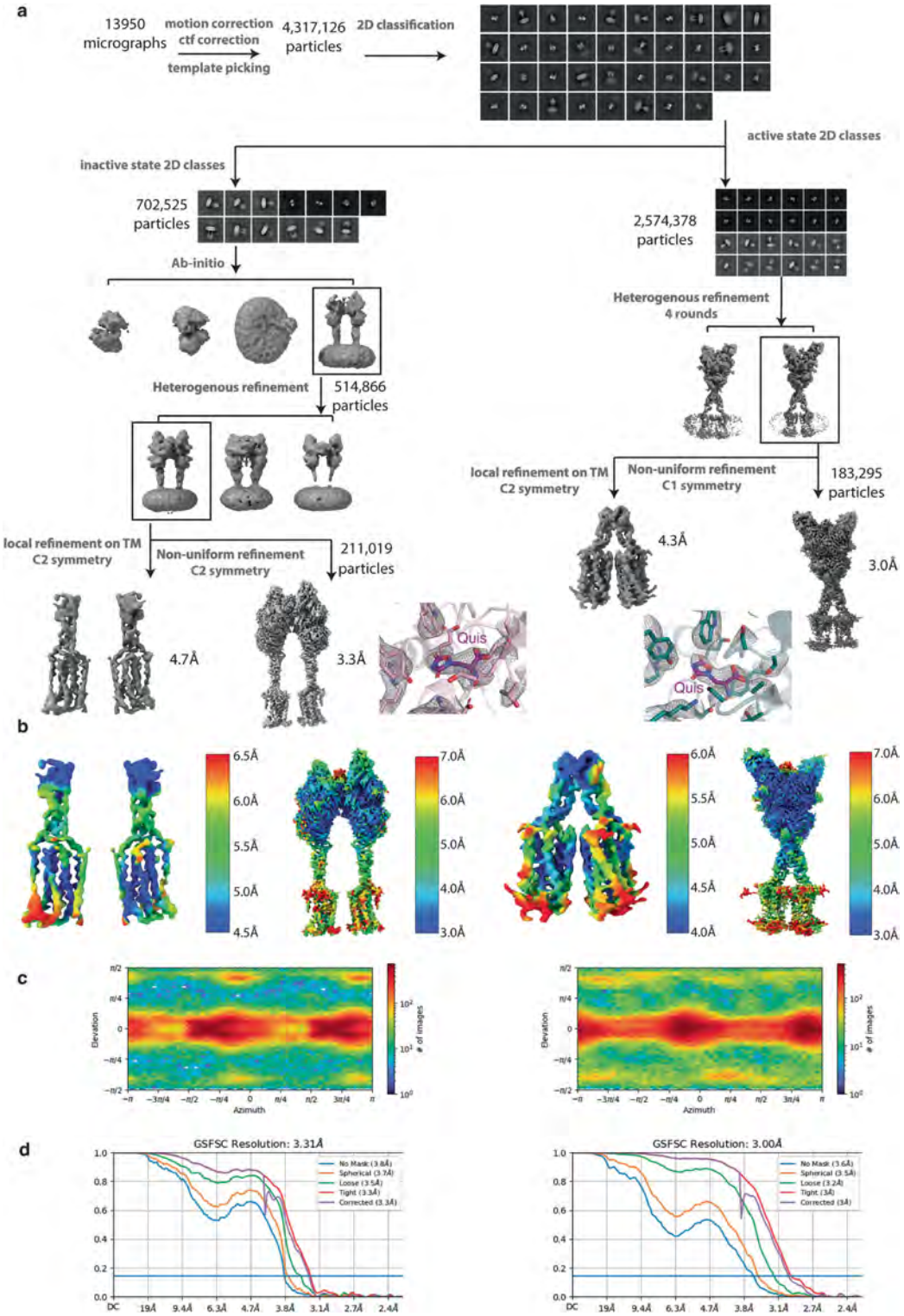

Extended Data Fig. 3 | Cryo-EM data processing workflow and resolution assessment of Quis-bound maps. (a) Workflow of cryo-EM data processing to obtain Quis-bound Intermediate 1a and Quis-bound Intermediate 2a structures. Also shown is the density for Quis and residues around the ligand in the two structures. (b) Local resolution maps of the Quis-bound structures. (c) Angular particle distribution of the Quis-bound structures. (d) Gold-standard FSC curves of the structures.

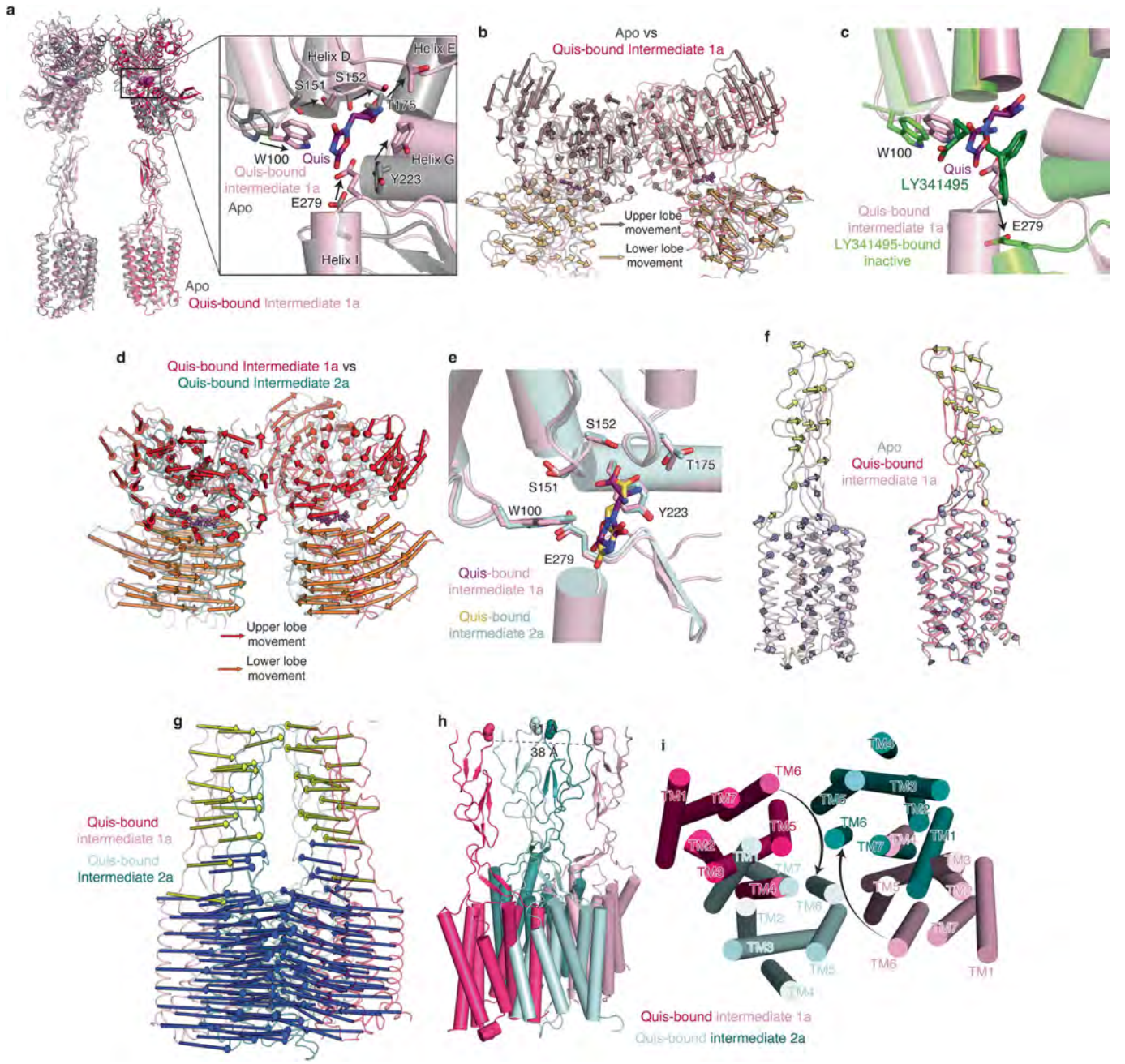

Extended Data Fig. 4 | Comparison of mGlu5 structures upon activation by Quis. (a) Overlay of the Apo (grey, PDB: 6N52) and Quis-bound Intermediate 1a showing CRDs and TMDs in an "inactive" state. Insert shows the Quis binding pocket. (b) Movement of the VFTs upon agonist binding in Quis-bound Intermediate 1a state compared to the Apo state (PDB 6N52, grey). Arrows represent the movement of every 5 Cα atoms from the Apo to the Intermediate 1a state upon Quis binding. Nb43 is shown in yellow. (c) To get insights into structural changes needed to initiate activation, we compared the Quis-bound Intermediate 1a (light pink) and the antagonist, LY341495-bound (PDB: 7FD9, dark green) mGlu5 structures. LY341495 binding to the receptor inhibits the movement of residues W100 and E279. (d) Comparing the movement of the VFTs in the Quis-bound Intermediate 1a (light pink, magenta) and the Quis-bound Intermediate 2a states (cyan and teal) show large rearrangements in the lower lobe, with relatively smaller changes in the upper lobe. Arrows represent the movement of every 5 Cα atoms from the Intermediate 1a state to the Intermediate 2a state. (e) Single protomer alignment of Quis-bound Intermediate 2a (cyan) and Quis-bound Intermediate 1a (light pink) structures show no change in the Quis binding pocket. (f) Overlay of Apo (grey, PDB: 6N52) and Quis-bound Intermediate 1a states show minimal changes in the CRDs and TMs. Arrows represent the movement of every 5 Cα atoms from Apo to Intermediate 1a. (g) Large changes in the CRDs and TMs are seen when comparing the Quis-bound Intermediate 1a and the Quis-bound Intermediate 2a states. Arrows represent the movement of every 5 Cα atoms from Intermediate 1a state to Intermediate 2a. (h) The CRDs in the Quis-bound Intermediate 1a structure are separated by ~38 Å (as measured at residue E527). In the Quis-bound Intermediate 2a state, the twisting of the lower lobe enables the CRDs (~11 Å at residue E527) and TMs to move adjacent to each other. (i) The TMs in the Quis-bound Intermediate 1a structure are far apart with TM5 being the most proximal helix pair (~21 Å). In the Quis-bound Intermediate 2a state the TMs of the protomers, in addition to moving closer to each other, rotate ~20° to form a TM6-TM6 interface, a hallmark of Family C activation.

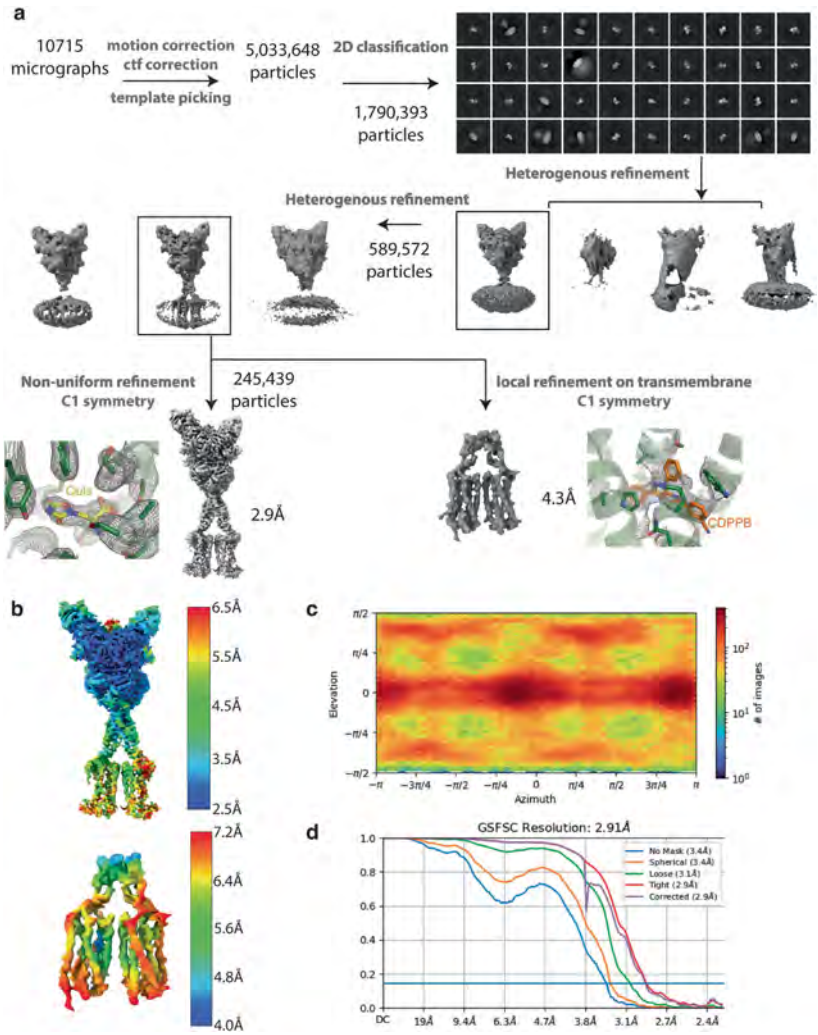

Extended Data Fig. 5 | Cryo-EM data processing workflow and resolution assessment of CDPPB, Quis-bound map. (a) Workflow of cryo-EM data processing to obtain CDPPB, Quis-bound mGlu5 structure, Intermediate 3a. Also shown is the density for Quis and CDPPB, with density also shown for residues around the ligands. (b) Local resolution maps of the CDPPB, Quis-bound mGlu5 structure. (c) Angular particle distribution of the structure. (d) Gold-standard FSC curves of the Quis-bound mGlu5 structure.

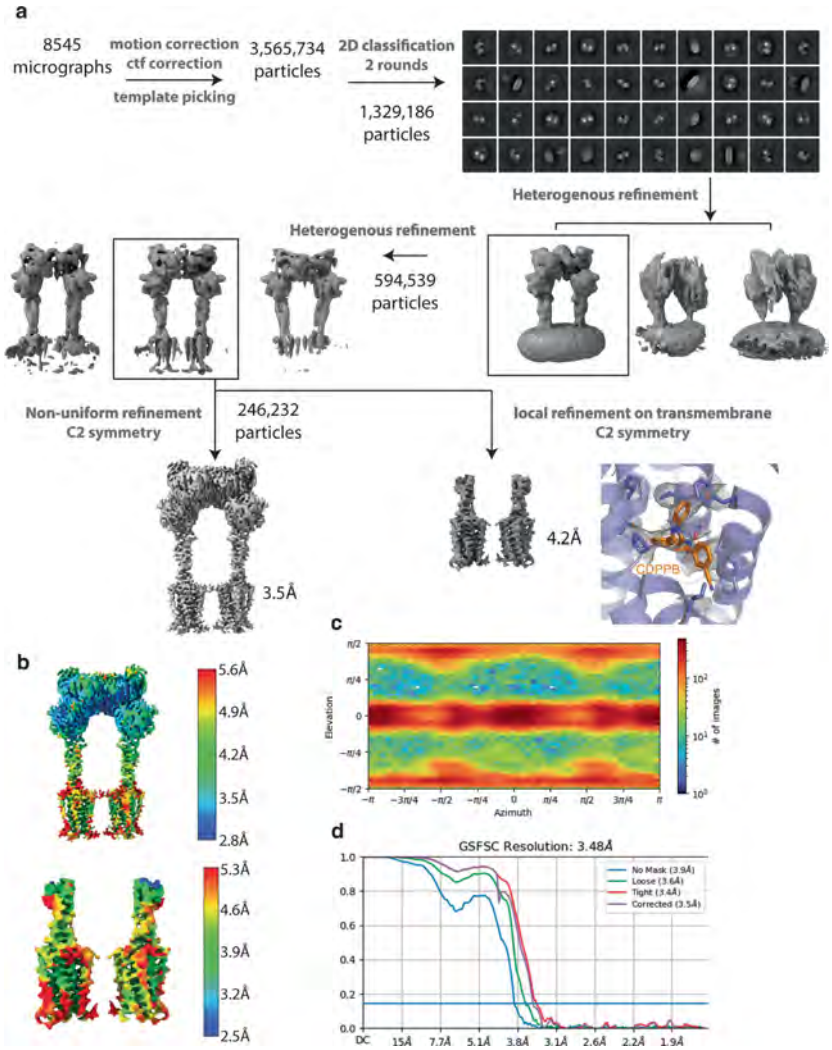

Extended Data Fig. 6 | Cryo-EM data processing workflow and resolution assessment of CDPPB-bound map. (a) Workflow of cryo-EM data processing to obtain CDPPB-bound mGlu5 Intermediate1b structure. The density of CDPPB and the residues around the ligand are shown. (b) Local resolution maps of the CDPPB-bound mGlu5 structure. (c) Angular particle distribution of the structure. (d) Gold-standard FSC curves of the CDPPB-bound mGlu5 structure.

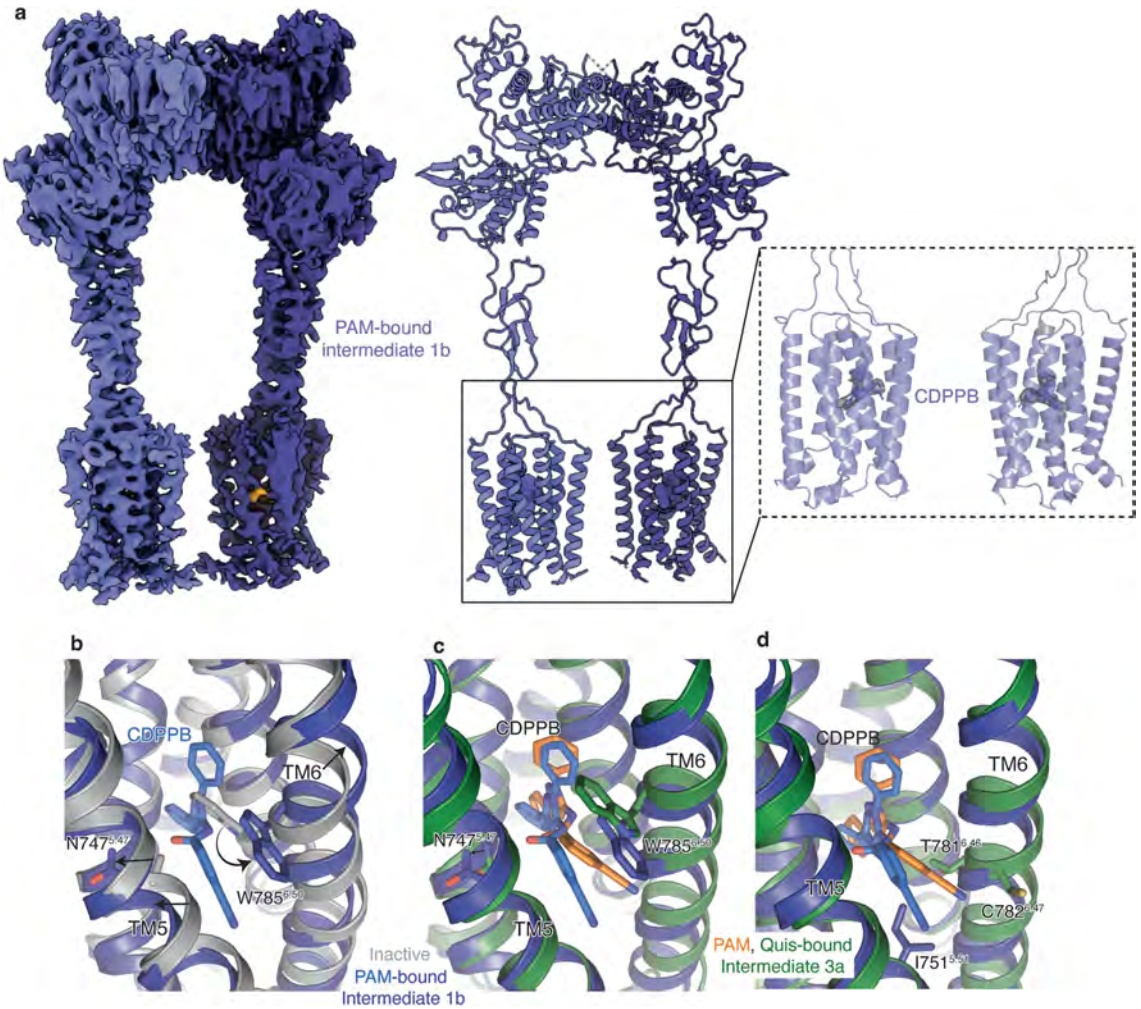

Extended Data Fig. 7 | CDPPB-bound structure analysis. (a) Cryo-EM density and model of CDPPB-bound mGlu5 Intermediate 1b in a nanodisc. Also shown is the density for the two bound CDPPB, one in each TM domain. (b) Comparison of the allosteric binding pocket in Apo (PDB:6N52, grey) and CDPPB-bound mGlu5 (dark blue), shows changes in TM5 ($N747^{5.47}$) and TM6 ($W785^{6.50}$) to accommodate CDPPB (slate). (c) Overlay of CDPPB from Intermediate 1b (dark blue) and Intermediate 3a structures showing minimal changes in the conformation of TM5 and TM6. (d) Residues that interact with CDPPB only in Intermediate 3a are shown in green ($T781^{6.46}$ and $C782^{6.47}$) and those that interact with CDPPB only in Intermediate 1b are shown in blue ($I751^{5.51}$).

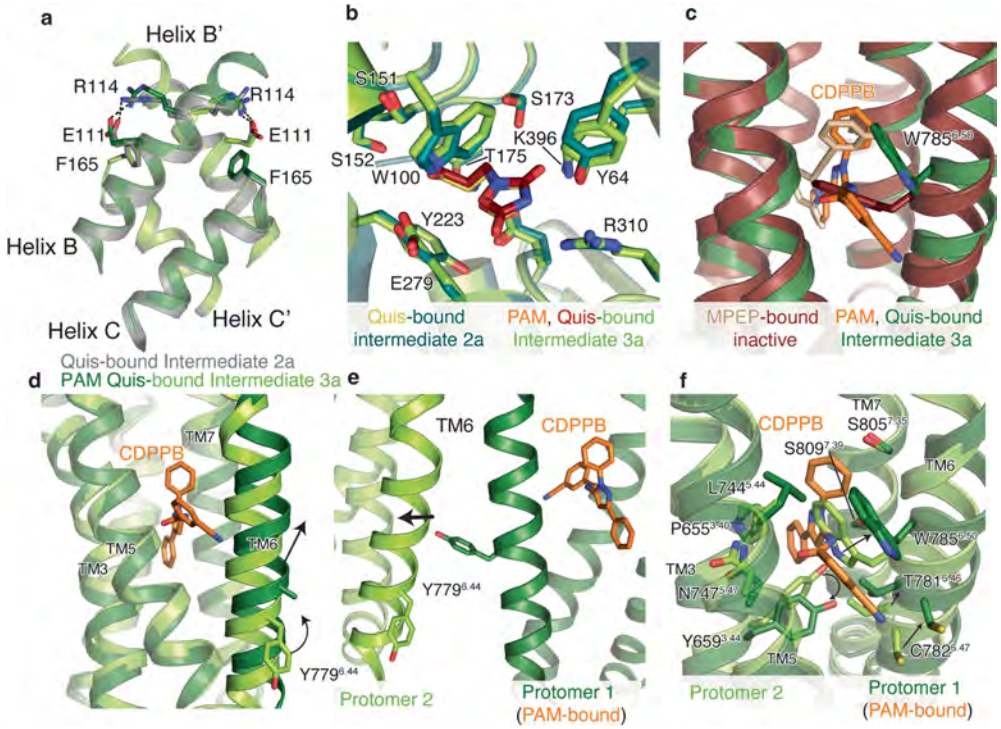

Extended Data Fig. 8 | CDPPB, Quis-bound structural analysis. (a) Overlay of intersubunit B and C helices in Quis-bound Intermediate 2a state and CDPPB, Quis-bound Intermediate 3a structure. Residues R114 and E111 interact in both structures. (b) Overlay of Quis binding pocket in Quis-bound Intermediate 2a and CDPPB, Quis-bound Intermediate 3a structures, showing no difference in the ligand pocket. (c) The conformation of residue W785$^{6.50}$ is different in the structure with the NAM, MPEP (PDB: 6FFI, brown) compared to that with the PAM, CDPPB (dark green). (d) TM6 in the CDPPB-bound Protomer 1 has moved outward compared to Protomer 2 with no CDPPB bound. In CDPPB-bound Protomer 1, Y779$^{6.44}$ points towards the intersubunit interface, as seen in (e). Though we cannot model the Y779$^{6.44}$ sidechain in Protomer 1 with confidence due to a lack of good density, we have added the most frequently occurring rotomer of Tyr. (f) Comparison of the allosteric pocket in CDPPB-bound protomer (protomer 1, dark green and CDPPB shown as orange) and the protomer with no CDPPB (protomer 2, green).

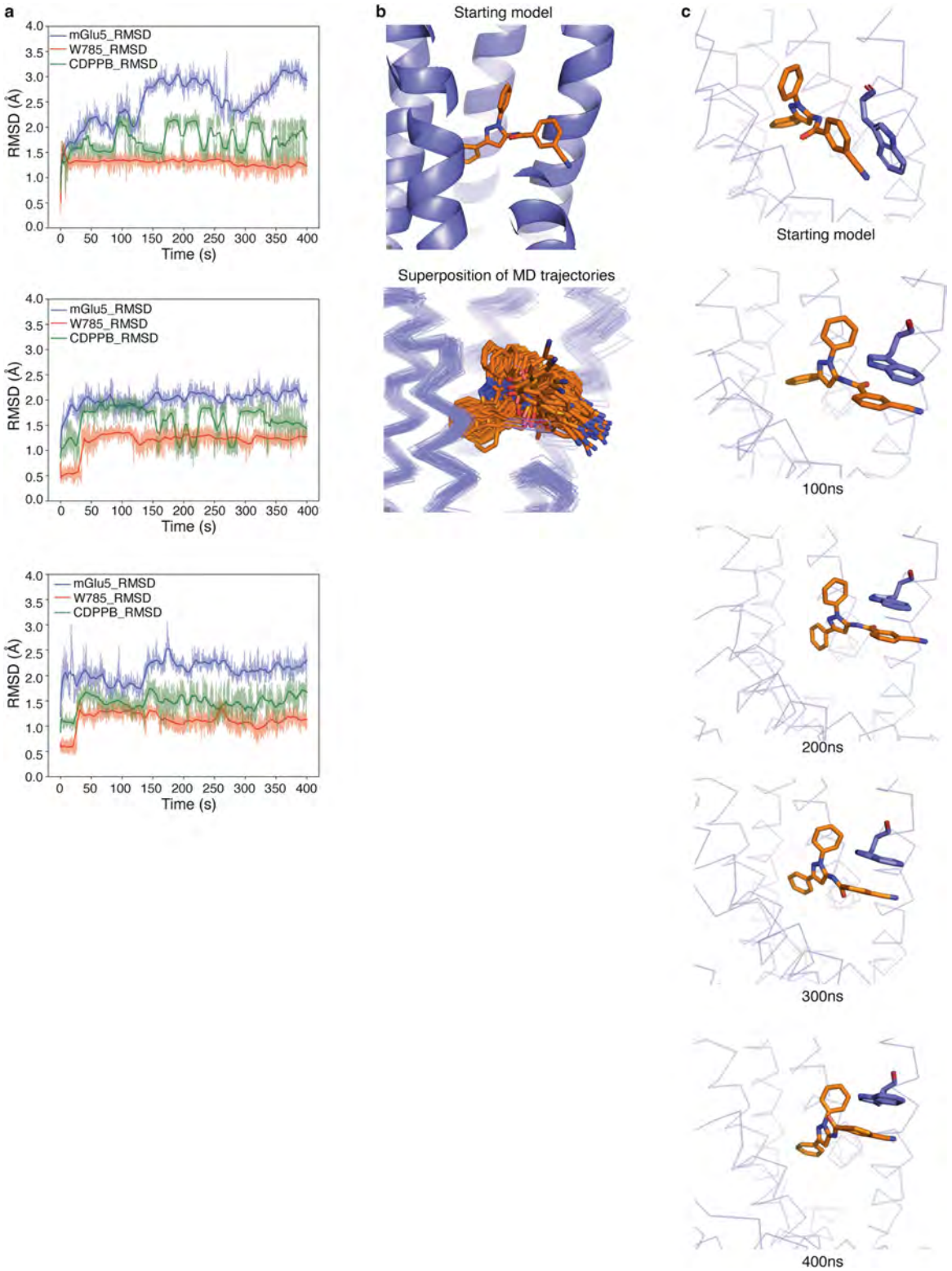

Extended Data Fig. 9 | Molecular Dynamics (MD) simulations of CDPPB. (a) Three replicates of the MD trajectories showing the RMSD of mGlu5 (blue), of the residue W785$^{6.50}$ (red) and CDPPB (green). Data represented as mean ± s.e.m. (b) The Starting model and the MD trajectory superpositions are shown. (c) Snapshots of the CDPPB and W785$^{6.50}$ every 100 ns is shown.

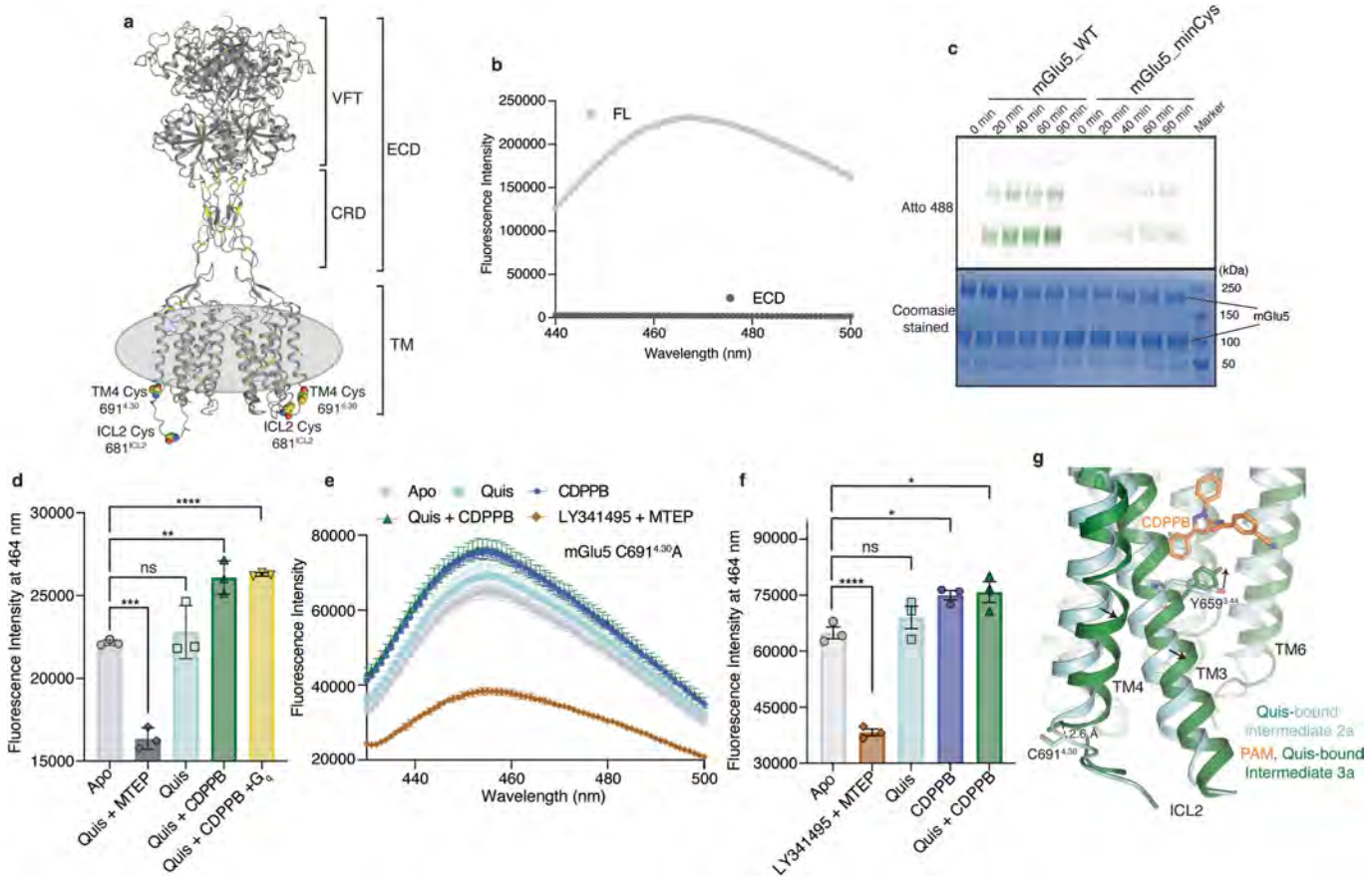

Extended Data Fig. 10 | Characterisation of minimal cysteine mGlu5 and ICL2 conformation. (a) Residues Cys691$^{4.30}$ and Cys681^{ICL2} that contribute to background labeling with dyes are shown as spheres. Other cysteine residues in the receptor are shown as yellow sticks. (b) mGlu5 full-length and ECD alone (VFT and CRD) were labeled with the cysteine reactive dye, monobromobimane. Though no signal was seen for ECD (dark grey), full-length (FL) mGlu5 produced a bimane spectrum (light grey). This implies that mGlu5 TMs have cysteine residues that are exposed to being labeled with bimane. n = 1 individual experiment. (c) WT and minimal cysteine (C691$^{4.30}$A and C681^{ICL2}A) constructs were labeled with Atto488. Unlike WT, the minimal cysteine construct exhibits almost no background labeling for the times tested (for gel source data, see Supplementary Fig. 1b). (d) Fluorescence intensity at 464 nm for mGlu5 WT labeled with bimane (reading out on ICL2 conformation from Fig. 3d) is plotted for the different ligand conditions. Though there is no significant difference between Apo (light grey) and Quis (cyan), the addition of Quis and CDPPB (dark green) showed a significant change. No further change was detected with the addition of G_q to the Quis and CDPPB condition (yellow). The addition of MTEP resulted in a significant decrease in fluorescence intensity (dark grey). Data represented as mean ± s.d., ns = 0.5326, p = 0.0001***, p = 0.0026**, p < 0.0001****, unpaired t-test (two-tailed) performed for statistical analysis between two conditions. One-way ANOVA performed for comparison across multiple conditions showed p < 0.0001, n = 3 individual experiments. (e) Bimane spectra of mGlu5 in nanodiscs labeled only at C681^{ICL2} (C691$^{4.30}$A construct). Unlike adding Quis (cyan) which resulted in no change in the spectrum, the addition of CDPPB alone (blue) or Quis and CDPPB (dark green) increases the fluorescence. On the other hand, LY341495 and MTEP (brown) cause a decrease in fluorescence. Data represented as mean ± s.e.m., n = 3 individual experiments. (f) Plotting the fluorescence intensity at 464 nm for bimane data in Extended Data Fig. 10e shows a significant difference between CDPPB alone (blue), Quis and CDPPB (dark green), and LY341495 and MTEP (brown) compared to Apo (grey). Data represented as mean ± s.e.m., ns = 0.5713, p < 0.0001, p = 0.0257* (Apo vs CDPPB), p < 0.0160* (Apo vs Quis + CDPPB), unpaired t-test (two-tailed) performed for statistical analysis between two conditions. One-way ANOVA performed for comparison across multiple conditions showed p < 0.0001, n = 3 individual experiments. (g) Comparison of Quis-bound (cyan) and CDPPB, Quis-bound structures (dark green) showing changes in TM3 and TM4 (~2.6 Å). Also shown is the position of residue C691$^{4.30}$ which is bimane labeled in the WT construct (Fig. 3d, Extended Data Fig. 10e).

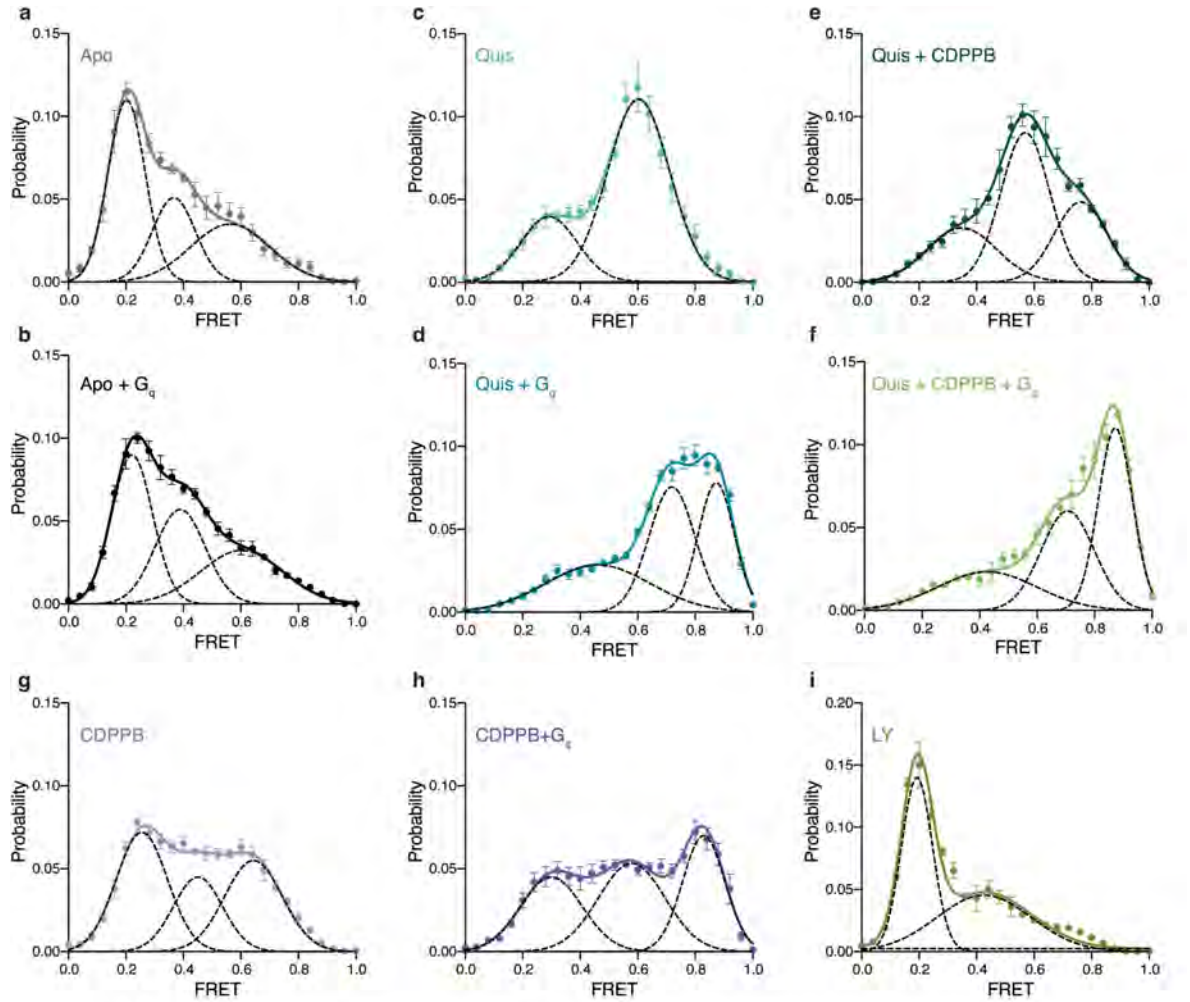

j % Area under each of the three Gaussian fits to FRET distribution in (a)-(i) (center of peak i.e. mean of gaussian)

FRET Peak \ Condition	Apo	Apo + G_q	Quis	Quis + G_q	Quis + CDPPB	Quis + CDPPB + G_q	CDPPB	CDPPB + G_q	LY
~ 0.25	45.2 (0.20)	45.1 (0.22)	24.3 (0.29)				40.7 (0.25)	29.9 (0.30)	50.6 (0.19)
~ 0.40	24.3 (0.37)	31.1 (0.39)		32.1 (0.46)	24.6 (0.35)	24.9 (0.43)	31.1 (0.39)		49.4 (0.42)
~ 0.60	30.6 (0.56)	28.8 (0.60)	75.6 (0.6)		47.8 (0.57)		34.9 (0.64)	28.5 (0.58)	
~ 0.75				37.5 (0.72)	27.6 (0.76)	34.6 (0.71)			
~ 0.90				30.4 (0.87)		40.4 (0.87)		31.6 (0.83)	

Extended Data Fig. 11 | Fractional occupancy determined from FRET histograms with three component Gaussian fits. (a) – (i) FRET histogram with three component Gaussian fits for each ligand condition. (j) Percentage area under the peak and peak center values. Apo (n = 319), Quis (n = 392), Quis + CDPPB (n = 329), Quis + G_q (n = 306), Quis + CDPPB + G_q (n = 317), LY341495 (LY) (n = 245), CDPPB (n = 329) and CDPPB + G_q (n = 347). Data represented as mean ± s.e.m.

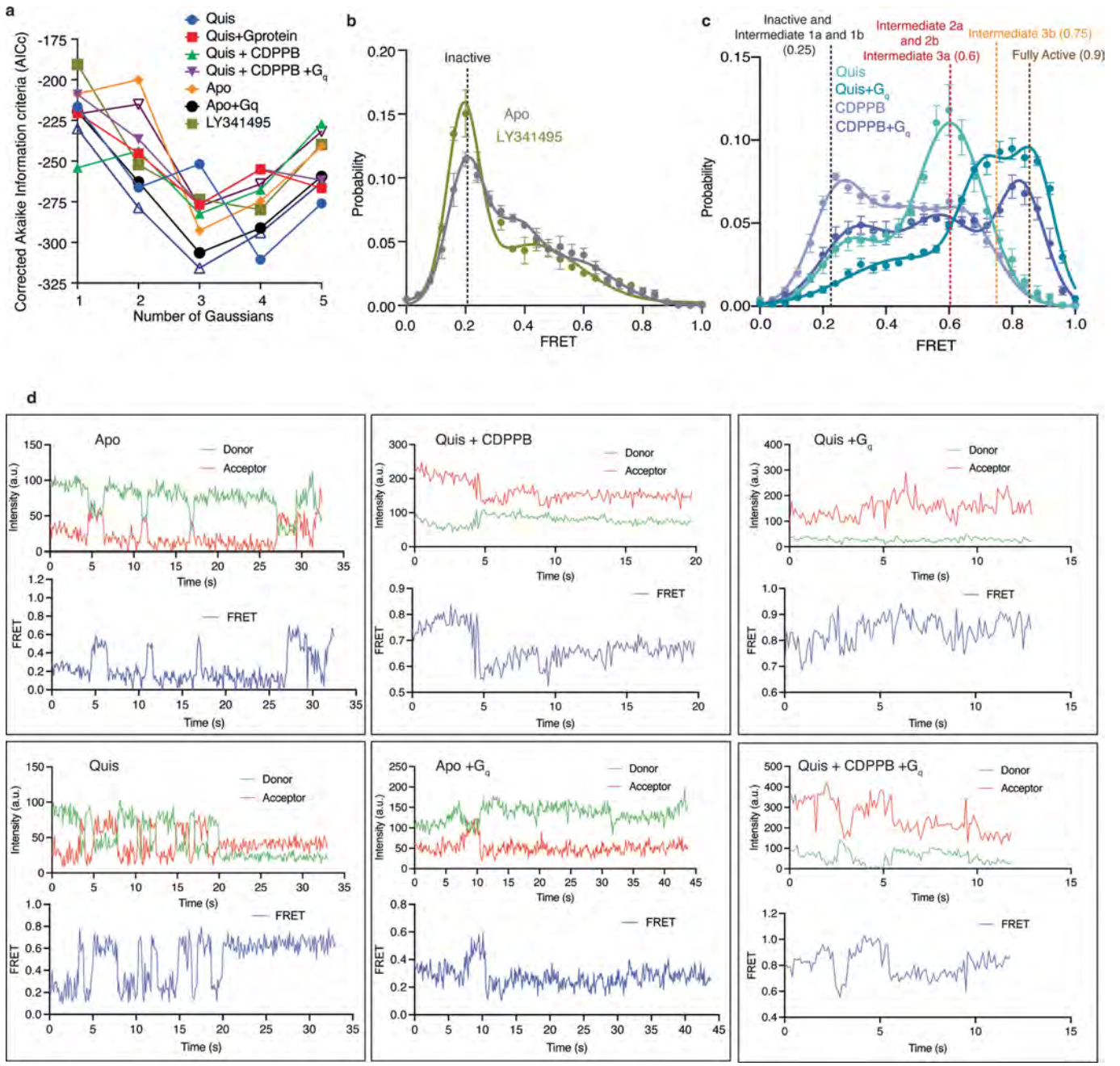

Extended Data Fig. 12 | smFRET fitting statistics and analysis. (a) Plot of the Akaike information criterion (corrected for small sample size, AICc) values for analysis with 1 to 5 Gaussians fits for the smFRET data. The AICc values showed broad minima at 3 and 4 fits. Three Gaussians were used to fit the data. (b) smFRET data showing the comparison of Apo (grey, n = 319) and antagonist-bound mGlu5 (brown, n = 245). Data represented as mean ± s.e.m. (c) The addition of CDPPB alone results in two FRET peaks, one at 0.25, Intermediate 1b state, and the other at 0.6, the Intermediate 2b state (slate, n = 329). In the presence of Quis (teal), the same two FRET peaks are seen except with different relative proportions of the two states. The addition of G_q to the Quis-alone sample shifts the population to the high FRET states, Intermediate 3b (0.75) and Fully Active (0.9) at the expense of the Intermediate 2a (0.6) and Intermediate 1a (0.25) peaks. For the CDPPB alone sample, the addition of G_q results in the appearance of a high FRET peak with a decrease, but not complete disappearance of the Intermediate 2b (0.6) and Intermediate 1b (0.25) peaks (n = 347). Data represented as mean ± s.e.m. (d) Example smFRET traces showing donor (green), and acceptor (red) intensity values as well as the calculated FRET values (blue) for a series of ligand conditions with and without G_q.

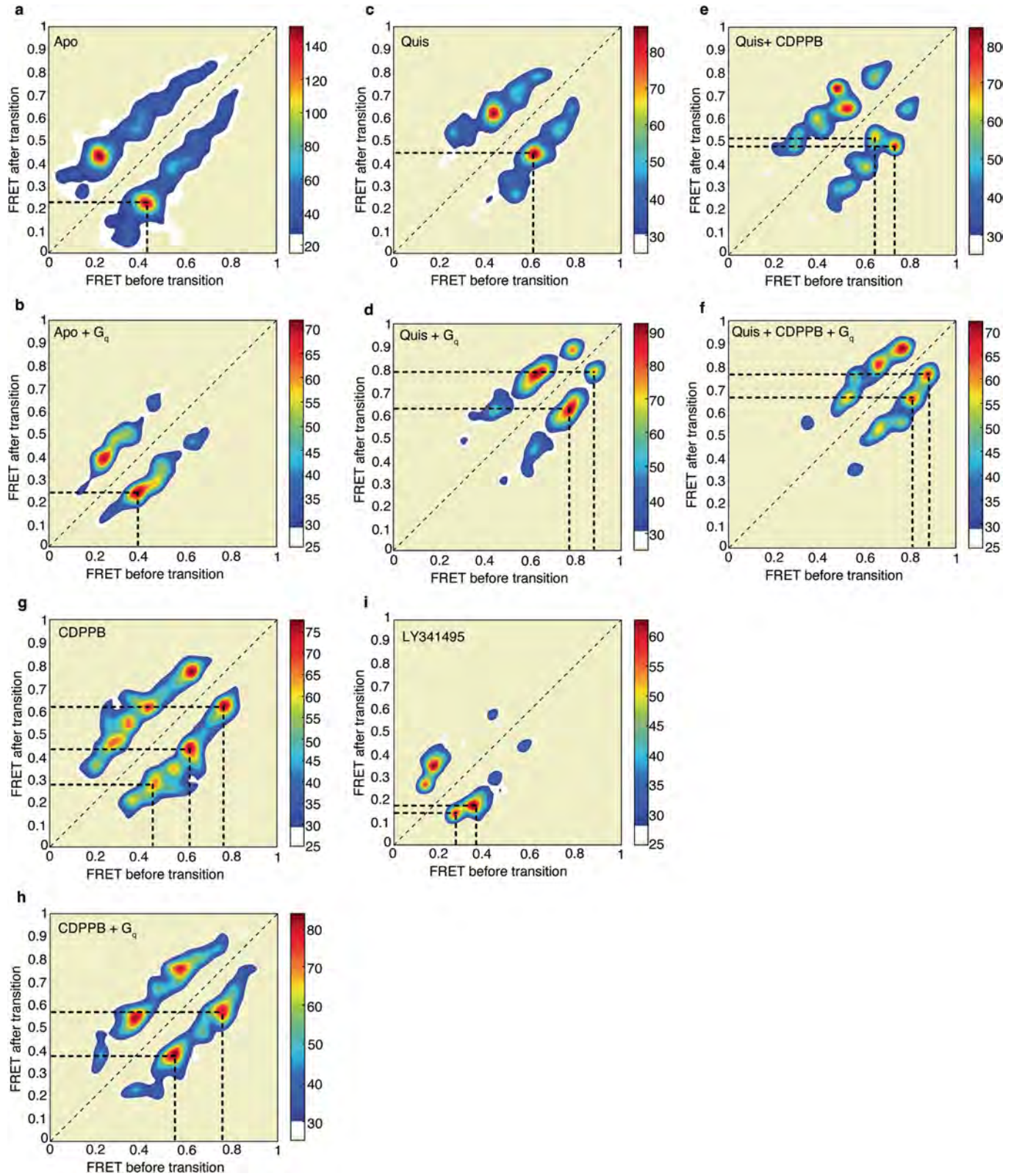

Extended Data Fig. 13 | Transition Density plots for different ligand conditions. (a) In the Apo state, we see transitions between the 0.25 and 0.4 FRET states. (b) With the addition of G_q, we see higher FRET state transitions, in addition to the 0.25 to 0.4 transitions. (c) In the presence of Quis, we see transitions between 0.4 and 0.6 FRET states. (d) Adding G_q to Quis-bound mGlu5 results in transitions between 0.6 and 0.75 states and between 0.75 and 0.9 states. No transition is seen between 0.6 and 0.9 states, indicating a stepwise transition from 0.6 to 0.75 to 0.9 states. (e) With Quis and CDPPB, transitions are seen between 0.4 and 0.6 and between 0.6 and 0.75 FRET states. Also, there are off-diagonal transitions between 0.4 and 0.75 states, indicating that CDPPB lowers the energy of the 0.75 state so that the 0.4 to 0.75 transitions can occur. This 0.4 to 0.75 transition is not seen with other ligand conditions. (f) Adding G_q to Quis and CDPPB results in more 0.6 to 0.75 transitions and the appearance of the 0.75 to 0.9 transitions. (g) CDPPB alone results in mostly transitions between 0.25 and 0.4, 0.4 and 0.6 and 0.6 and 0.75 FRET states. (h) Adding G_q to CDPPB results in higher FRET transitions, in addition to 0.4 to 0.6 and 0.6 to 0.75 transitions. The transition of 0.25 to 0.4 FRET state is minimal. (i) In LY341495, we see low FRET state transitions, indicating stabilization of inactive states.

Extended Data Table 1 | Cryo-EM data collection, refinement and validation statistics

	CDPPB bound inactive mGlu5 (EMDB-41069) (PDB 8T6J)	Quis bound intermediate mGlu5-Nb43 (EMDB-41092) (PDB 8T7H)	Quis bound active mGlu5-Nb43 (EMDB-41099) (PDB 8T8M)	Quis+CDPPB bound active mGlu5-Nb43 (EMDB-41139) (PDB 8TAO)
Data collection and processing				
Magnification	107000	82000	82000	82000
Voltage (kV)	300	300	300	300
Electron exposure (e–/Å²)	52.2	50	50	51.6
Defocus range (μm)	0.7-2	0.7-2	0.7-2	0.7-2
Pixel size (Å)	0.8521	1.111	1.111	1.111
Symmetry imposed	C2	C2	C2	C1
Initial particle images (no.)	3,565,734	4,317,126	4,317,126	5,033,648
Final particle images (no.)	246,232	211,019	183,295	245,439
Map resolution (Å)	3.5	3.3	3.0	2.9
FSC threshold	0.143	0.143	0.143	0.143
Map resolution range (Å)	2.8-5.6	3.0-7.0	3.0-7.0	2.5-7.2
Refinement				
Initial model used (PDB code)	6N52	6N51 and 6N52	6N51	6N51
Model resolution (Å)	3.4	3.5	3.2	3.1
FSC threshold	0.5	0.5	0.5	0.5
Model resolution range (Å)	31.6-3.4	38.5-3.5	42.6-3.2	2.9-3.1
Map sharpening *B* factor (Å²)	-22.85	-59.41	-25.33	-51.06
Model composition				
Non-hydrogen atoms	11652	13100	13146	13422
Protein residues	1534	1794	1770	1794
Ligands	2	2	2	3
B factors (Å²)				
Protein	60.67	30.43	36.58	45.08
Ligand	55.65	17.07	11.77	46.72
R.m.s. deviations				
Bond lengths (Å)	0.002	0.003	0.003	0.002
Bond angles (°)	0.579	0.597	0.534	0.509
Validation				
MolProbity score	1.69	1.73	1.64	1.48
Clashscore	6.09	7.94	6.10	4.70
Poor rotamers (%)	0.00	0.00	0.00	0.00
Ramachandran plot				
Favored (%)	94.88	95.73	95.66	96.40
Allowed (%)	5.12	4.27	4.34	3.60
Disallowed (%)	0.00	0.00	0.00	0.00

nature portfolio

Corresponding author(s): Kaavya Krishna Kumar and Brian Kobilka

Last updated by author(s): Mar 4, 2024

Reporting Summary

Nature Portfolio wishes to improve the reproducibility of the work that we publish. This form provides structure for consistency and transparency in reporting. For further information on Nature Portfolio policies, see our Editorial Policies and the Editorial Policy Checklist.

Statistics

For all statistical analyses, confirm that the following items are present in the figure legend, table legend, main text, or Methods section.

n/a	Confirmed	
☐	☒	The exact sample size (*n*) for each experimental group/condition, given as a discrete number and unit of measurement
☐	☒	A statement on whether measurements were taken from distinct samples or whether the same sample was measured repeatedly
☐	☒	The statistical test(s) used AND whether they are one- or two-sided *Only common tests should be described solely by name; describe more complex techniques in the Methods section.*
☒	☐	A description of all covariates tested
☒	☐	A description of any assumptions or corrections, such as tests of normality and adjustment for multiple comparisons
☐	☒	A full description of the statistical parameters including central tendency (e.g. means) or other basic estimates (e.g. regression coefficient) AND variation (e.g. standard deviation) or associated estimates of uncertainty (e.g. confidence intervals)
☐	☒	For null hypothesis testing, the test statistic (e.g. *F*, *t*, *r*) with confidence intervals, effect sizes, degrees of freedom and *P* value noted *Give P values as exact values whenever suitable.*
☒	☐	For Bayesian analysis, information on the choice of priors and Markov chain Monte Carlo settings
☒	☐	For hierarchical and complex designs, identification of the appropriate level for tests and full reporting of outcomes
☒	☐	Estimates of effect sizes (e.g. Cohen's *d*, Pearson's *r*), indicating how they were calculated

Our web collection on statistics for biologists contains articles on many of the points above.

Software and code

Policy information about availability of computer code

Data collection	CryoEM Data was collected on a Titan Krios (FEI)
Data analysis	FluorEssence v3.8, MotionCor2, CTFFIND4, RELION 3.1, cryosparc 3.3.2, phenix 1.19.2, UCSF Chimera 1.15, Coot 0.8.9, GraphPad Prism 9, PyMOL 2.5.4, HD-Examiner 3.1, SPARTAN 3.7, CHARMM36m, OpenMM, MDAnalysis 3.1, vbFRET, Maestro 2021-1

For manuscripts utilizing custom algorithms or software that are central to the research but not yet described in published literature, software must be made available to editors and reviewers. We strongly encourage code deposition in a community repository (e.g. GitHub). See the Nature Portfolio guidelines for submitting code & software for further information.

Data

Policy information about availability of data

All manuscripts must include a data availability statement. This statement should provide the following information, where applicable:

- Accession codes, unique identifiers, or web links for publicly available datasets
- A description of any restrictions on data availability
- For clinical datasets or third party data, please ensure that the statement adheres to our policy

The PDB codes for the four structures described in this manuscript: 8T7H, 8T8M, 8TAO, 8T6J.
The EMDB codes for the four structures in this manuscript: EMDB-41092, EMDB-41099, EMDB-41139 and EMDB-41069.

The PDB codes of available structures mentioned in the manuscript are: 6N50, 6N51, 6N52, 7FD9, 6N4Y, 6FFI, 7MTR, 7MTS
EMDB codes of available structures mentioned in this manuscript: EMDB-0345 or EMDB-0346

Human research participants

Policy information about studies involving human research participants and Sex and Gender in Research.

Reporting on sex and gender	Not applicable
Population characteristics	Not applicable
Recruitment	Not applicable
Ethics oversight	Not applicable

Note that full information on the approval of the study protocol must also be provided in the manuscript.

Field-specific reporting

Please select the one below that is the best fit for your research. If you are not sure, read the appropriate sections before making your selection.

☒ Life sciences ☐ Behavioural & social sciences ☐ Ecological, evolutionary & environmental sciences

For a reference copy of the document with all sections, see nature.com/documents/nr-reporting-summary-flat.pdf

Life sciences study design

All studies must disclose on these points even when the disclosure is negative.

Sample size	For the functional data atleast three independent replicates were carried out, which was enough to perform statistical analysis.
Data exclusions	No data were excluded.
Replication	Atleast three independent experiments were conducted for the functional assays. All attempts at replication were successful.
Randomization	In the Fourier shell correlation (FSC) measurement in CryoSPARC 3.3.2 data processing pipeline, data were randomly divided into two halves resulting in two independently determined 3D volumes that were used for the FSC calculation.
Blinding	Since no subjective assessment was required, blinding was not required.

Reporting for specific materials, systems and methods

We require information from authors about some types of materials, experimental systems and methods used in many studies. Here, indicate whether each material, system or method listed is relevant to your study. If you are not sure if a list item applies to your research, read the appropriate section before selecting a response.

Materials & experimental systems

n/a	Involved in the study
☒	☐ Antibodies
☐	☒ Eukaryotic cell lines
☒	☐ Palaeontology and archaeology
☒	☐ Animals and other organisms
☒	☐ Clinical data
☒	☐ Dual use research of concern

Methods

n/a	Involved in the study
☒	☐ ChIP-seq
☒	☐ Flow cytometry
☒	☐ MRI-based neuroimaging

Eukaryotic cell lines

Policy information about cell lines and Sex and Gender in Research

Cell line source(s)	Sf9, Expression Systems, Cat 94-001S. Tni Cells (Hi-5), Expression Systems, Cat 94011S. Inducible Expi293 cells, Thermo Scientific, Cat A39251

Authentication	Cell lines are maintained by the supplier. No additional authentication was performed by the authors of this study
Mycoplasma contamination	Cell lines are tested by manufacturer for contamination, but were not further tested by the authors of this study.
Commonly misidentified lines (See ICLAC register)	No commonly misidentified lines were used in this study.